

Compliance Minimization via Physics-Informed Gaussian Processes

Xiangyu Sun¹, Amin Yousefpour¹, Shirin Hosseinmardi¹, and Ramin Bostanabad^{*1,2}

¹Department of Mechanical and Aerospace Engineering, University of California, Irvine

²Department of Civil and Environmental Engineering, University of California, Irvine

Abstract

Machine learning (ML) techniques have recently gained significant attention for solving compliance minimization (CM) problems. However, these methods typically provide poor feature boundaries, are very expensive, and lack a systematic mechanism to control the design complexity. Herein, we address these limitations by proposing a mesh-free and simultaneous framework based on physics-informed Gaussian processes (GPs). In our approach, we parameterize the design and state variables with GP priors which have independent kernels but share a multi-output neural network (NN) as their mean function. The architecture of this NN is based on Parametric Grid Convolutional Attention Networks (PGCANs) which not only mitigate spectral bias issues, but also provide an interpretable mechanism to control design complexity. We estimate all the parameters of our GP-based representations by simultaneously minimizing the compliance, total potential energy, and residual of volume fraction constraint. Importantly, our loss function exclude all data-based residuals as GPs automatically satisfy them. We also develop computational schemes based on curriculum training and numerical integration to increase the efficiency and robustness of our approach which is shown to (1) produce super-resolution topologies with fast convergence, (2) achieve smaller compliance and less gray area fraction compared to traditional numerical methods, (3) provide control over fine-scale features, and (4) outperform competing ML-based methods.

Keywords: Gaussian Processes, Neural Networks, Topology Optimization, Compliance Minimization, Deep Energy Method.

1 Introduction

Topology optimization (TO) offers a powerful tool to determine the optimal material distribution and geometric features within a design domain by minimizing a specific objective function under a set of constraints. Since the pioneering work by [Bendsøe and Kikuchi \(1988\)](#), TO has gained significant attention across diverse applications in structural mechanics, fluid dynamics, and materials science ([Bendsøe, 1995](#); [Borrval and Petersson, 2003](#); [Bendsøe and Sigmund, 2004](#); [Wang et al., 2021](#)). Among various approaches, the solid isotropic material with penalization (SIMP) ([Sigmund, 2001](#); [Andreassen et al., 2011](#); [Liu and Tovar, 2014](#))

*Corresponding Author: raminb@uci.edu
[GitHub Repository](#)

and level-set methods (Chen et al., 2017) are the most widely adopted for structural optimization problems. In recent years, several advanced TO methods have been introduced to address increasingly complex design scenarios including multi-scale formulations (Wu et al., 2021; Zhao and Zhang, 2021; Zhai et al., 2024), local maximum stress constraints (Senhora et al., 2020), and considerations of fracture or plasticity (Jia et al., 2023). Among various applications, compliance minimization (CM) represents a foundational application case that provides a benchmark for evaluating and advancing new structural optimization methods. Using the finite element method (FEM) for modeling structural deformation with a linear elastic material, the standard SIMP formulation for CM is given as as:

$$\min_{\mathbf{u}_e, \rho_e} c(\mathbf{u}_e, \rho_e) = \sum_{e=1}^{N_e} (\rho_e)^p \mathbf{u}_e^T \mathbf{K}_0 \mathbf{u}_e \quad (1a)$$

$$\text{subject to } \frac{\sum_{e=1}^{N_e} \rho_e V_e}{\sum_{e=1}^{N_e} V_e} = \psi_f, \quad (1b)$$

$$\mathbf{K}\mathbf{U} = \mathbf{F}, \quad (1c)$$

$$\rho_{\min} \leq \rho_e \leq 1, \quad (1d)$$

where ρ_e , \mathbf{u}_e , \mathbf{K}_0 , V_e , and ψ_f ¹ denote the element density, nodal displacement vector, element stiffness matrix of the solid (i.e., phase 1), element volume, and prescribed volume fraction, respectively. The volume fraction constraint and the force equilibrium condition are enforced through Equation (1b) and Equation (1c), respectively. \mathbf{K} , \mathbf{U} and \mathbf{F} are the global stiffness matrix, global displacement vector, and global force vector, respectively. While optimizing element densities, a nonzero ρ_{\min} (typically set to 10^{-3}) is imposed to avoid numerical instabilities in inverting \mathbf{K} .

Most TO methods adopt a *nested* framework to solve the optimization problem in Equation (1) by coupling an analysis step with a design update step. In the analysis step, the state variables (i.e., nodal displacements) are obtained by solving Equation (1c) using FEM and then used to compute the objective function in Equation (1a) and the sensitivity field. The element densities are subsequently updated using gradient-based optimizers such as the optimality criteria (OC) method (Bendsøe, 1995) or the method of moving asymptotes (MMA) (Svanberg, 1987). Under static and linear elastic conditions, the SIMP method enables straightforward and efficient implementations (Sigmund, 2001; Andreassen et al., 2011) but it is prone to issues such as checkerboard patterns and mesh dependency which necessitate the use of filtering techniques such as gradient-based filters to regularize the solution. These filters, however, introduce some gray areas where element densities are not close to either 0 or 1.

Recent advancements in computational graphics have fueled the use of machine learning (ML) in TO (Shin et al., 2023). These ML-based approaches leverage various types of neural networks (NNs) and can be broadly categorized into two groups: (1) supervised data-driven approaches, and (2) unsupervised approaches based on physics-informed machine learning (PIML). Representative data-driven approaches have demonstrated significant acceleration in reducing computational costs by predicting sensitivity fields using trained ML models (Chi et al., 2021; Senhora et al., 2022). Generative models that can design optimal topologies in a single forward pass also belong to this category (Yamasaki et al., 2021; Sim et al., 2021; Kallioras and Lagaros, 2021; Nie et al., 2021). However, these methods heavily rely on large datasets generated by conventional methods such as SIMP or level-set and the generalization ability of these methods strongly depends on the size and quality of their training samples which are difficult to generate in many cases. Hence in this work, we focus on unsupervised physics-informed approaches.

¹We use non-italic symbols to denote variables, vectors, and matrices in the SIMP formulation based on FEM, while italic symbols are used in our mesh-free framework for differentiation.

PIML refers to a general class of ML models that are trained to surrogate a system’s state variables while leveraging domain knowledge which can be in the form of boundary/initial conditions (BCs/ICs) and the governing partial differential equations (PDEs). These BCs/ICs and the PDEs are typically included as loss terms and the training aims to minimize the corresponding residuals. In solid mechanics, the weak form of a PDE system is typically adopted and this practice has led to the development of the deep energy method (DEM) which minimizes the potential energy functional as opposed to the strong form of the force balance equilibrium (Nguyen-Thanh et al., 2020; He et al., 2023; Hamel et al., 2023). DEM has also been extended to accommodate nonlinear material behaviors and mixed formulations under large deformation scenarios (Nguyen-Thanh et al., 2020; Niu et al., 2023; He et al., 2023; Fuhg and Bouklas, 2022). Compared to PDE residuals, the variational weak form in DEM improves training stability and convergence rate.

Recent ML-based TO works have produced optimal topologies which are competitive to those obtained via SIMP. These works rely on one of the following three distinct strategies: (1) methods that parameterize the density field using NNs while relying on FEM solvers for displacement computations (Hoyer et al., 2019; Chandrasekhar and Suresh, 2021, 2022); (2) methods that estimate displacements using DEM while updating the density field via traditional optimizers such as OC or MMA (He et al., 2023; Yin et al., 2024; Zhao et al., 2024); and (3) fully ML-based frameworks that simultaneously parameterize displacement and density fields with separate NNs and update both minimizing an appropriately defined loss function whose derivatives can be easily obtained via automatic differentiation (AD) (Zehnder et al., 2021; Joglekar et al., 2024; Jeong et al., 2023). Although these three strategies differ methodologically, they all adopt a *nested* optimization framework in which displacement fields are repeatedly computed using either the FEM or the DEM during each design iteration. This *nested* structure leads to two potential issues: (1) FEM-based nested frameworks inherit limitations similar to those of the traditional SIMP method such as mesh dependency and computational overhead from repeated linear system solves, and (2) DEM-based methods are slow since the displacement field must be obtained by re-training the network (or part of it) at each design iteration. However, we argue that such a *nested* configuration is not strictly necessary: the design update step minimizes compliance and the analysis step minimizes potential energy, so both objectives can be simultaneously optimized. Such a simultaneous approach has the potential to improve computational efficiency while removing mesh sensitivity and gray area.

While ML-based TO frameworks have shown potential, their effectiveness heavily depends on the design of the NN architecture. The majority of existing works adopt feed-forward fully connected neural networks (also known as multilayer perceptrons or MLPs), which suffer from three major limitations: (1) spectral bias, where the network preferentially learns low-frequency components and struggles to capture sharp gradients or fine-scale features such as stress concentrations (Cuomo et al., 2022; Kang et al., 2023); (2) vanishing gradients in deep architectures, which reduces convergence rates and hinders effective loss minimization under the adjoint framework; and (3) difficulty in strictly enforcing BCs and design constraints on the density field, where reliance on residual loss terms increases training complexity and distorts the optimization trajectory.

In this work we develop a simultaneous and mesh-free framework for CM based on physics-informed Gaussian processes (GPs). In our framework, we parametrize the displacement and density variables with GP priors with independent kernels but a shared multi-output mean function (the number of outputs equals to the total number of design and state variables). We develop a physics-based loss function to estimate the parameters of our formulation and, in turn, obtain a continuous representation of the displacement and density fields. Our framework produces topologies with minimal gray areas and has interpretable mechanisms for controlling the complexity of the designed topologies or enforcing design constraints.

We design the mean function of our parameterization via a unique NN architecture, i.e., a parametric grid convolution attention network (PGCAN). This architecture mitigates the spectral bias of MLPs and can

capture solutions with high gradients (e.g., stress concentrations) which are critical to CM problems. We estimate the parameters of our PGCAN by minimizing an appropriately defined loss function that combines multiple terms related to the compliance, total potential energy, and design constraints (e.g., desired volume fraction). This minimization is conducted robustly and efficiently via a gradient-based optimizer that leverages the adjoint method as well as adaptive numerical approximations and curriculum training.

The remainder of this paper is organized as follows. We review the fundamentals of the DEM in Section 2 and then introduce our approach in Section 3. Section 4 presents numerical results across various examples and methods including our approach, SIMP, and other ML-based methods. Section 5 concludes the paper and outlines potential directions for future research.

2 Deep Energy Method

The DEM offers an alternative to the FEM for solving displacement fields. For an isotropic linear elastic material in the absence of any body force, the governing PDE system is given by:

$$\nabla \cdot \boldsymbol{\sigma}(\mathbf{x}) = \mathbf{0}, \quad \forall \mathbf{x} \in \Omega, \quad (2)$$

where $\mathbf{x} = [x, y]^T$ denotes an arbitrary point in the 2D domain Ω and $\boldsymbol{\sigma}$ denotes the Cauchy stress tensor. We assume the boundary of the domain, i.e., $\partial\Omega = \partial\Omega_u \cup \partial\Omega_F$, is subjected to the following displacement and traction BCs:

$$u_i(\mathbf{X}_i) = \tilde{u}_i, \quad \forall \mathbf{X}_i \in \partial\Omega_u, \quad i = 1, 2, \quad (3a)$$

$$\boldsymbol{\sigma}(\mathbf{X}_F) \cdot \mathbf{n}(\mathbf{X}_F) = \mathbf{F}, \quad \forall \mathbf{X}_F \in \partial\Omega_F, \quad (3b)$$

where $\mathbf{u}(\mathbf{x}) = [u_1(\mathbf{x}), u_2(\mathbf{x})]^T$ is the displacement vector, the two-column matrices \mathbf{X}_i and \mathbf{X}_F represent sets of spatial points where the displacement and traction BCs are specified, respectively, \tilde{u}_i is the vector specifying the displacement BCs, $\mathbf{n}(\mathbf{x}) = [n_1(\mathbf{x}), n_2(\mathbf{x})]$ denotes the surface normal vector with two components, and \mathbf{F} is a matrix representing the external forces applied at \mathbf{X}_F . Assuming small deformations, the kinematic relationship between the strain tensor $\boldsymbol{\varepsilon}(\mathbf{x})$ and $\mathbf{u}(\mathbf{x})$ is given as:

$$\boldsymbol{\varepsilon}(\mathbf{x}) = \frac{1}{2}(\nabla \mathbf{u}(\mathbf{x}) + \nabla \mathbf{u}^T(\mathbf{x})), \quad (4)$$

where ∇ denotes the gradient operator defined as:

$$\nabla \mathbf{u}(\mathbf{x}) = \begin{bmatrix} \frac{\partial u_1(\mathbf{x})}{\partial x} & \frac{\partial u_1(\mathbf{x})}{\partial y} \\ \frac{\partial u_2(\mathbf{x})}{\partial x} & \frac{\partial u_2(\mathbf{x})}{\partial y} \end{bmatrix}. \quad (5)$$

The linear elastic constitutive law in tensor form is written as:

$$\boldsymbol{\sigma}(\mathbf{x}) = \mathbf{C} : \boldsymbol{\varepsilon}(\mathbf{x}), \quad (6)$$

where \mathbf{C} is the constant fourth-order elastic stiffness tensor, parameterized by the Young's modulus E and Poisson's ratio ν of the solid phase.

DEM is based on the principle of minimum potential energy, which asserts that a solid body in force equilibrium adopts the deformation state that minimizes the total potential energy among all kinematically admissible configurations. The total potential energy $L_P(\mathbf{u}(\mathbf{x}))$ is formulated as:

$$L_P(\mathbf{u}(\mathbf{x})) = \frac{1}{2} \int_{\Omega} \boldsymbol{\sigma}(\mathbf{x}) : \boldsymbol{\varepsilon}(\mathbf{x}) dV - \int_{\partial\Omega_F} \mathbf{f}^T(\mathbf{x}) \mathbf{u}(\mathbf{x}) dA, \quad (7)$$

where $\mathbf{f}(\mathbf{x}) = [f_1(\mathbf{x}), f_2(\mathbf{x})]^T$ represents the external forces. The first term on the right-hand side of Equation (7) quantifies the strain energy and the second term accounts for the external work. So, instead of directly solving the strong form in Equation (2), in the DEM method the displacement field is parameterized by an NN whose loss function is based on Equation (7). This setup is schematically shown in Fig. 1 with an MLP whose outputs are denoted by $\mathbf{m}_u(\mathbf{x}, \boldsymbol{\theta}) = [m_{u_1}(\mathbf{x}, \boldsymbol{\theta}), m_{u_2}(\mathbf{x}, \boldsymbol{\theta})]^T$ where $\boldsymbol{\theta}$ denotes the trainable parameters.

In DEM, to ensure that the solution is kinematically admissible (i.e., satisfies the displacement BCs), either an extra residual loss term is included in the loss function, or a transformation such as the following is employed:

$$u_i(\mathbf{x}) = A_i(\mathbf{x}) + B_i(\mathbf{x})m_{u_i}(\mathbf{x}, \boldsymbol{\theta}), i = 1, 2, \quad (8)$$

where $A_i(\mathbf{x})$ and $B_i(\mathbf{x})$ are smooth and differentiable functions that satisfy $A_i(\mathbf{X}_i) = \tilde{\mathbf{u}}_i$ and $B_i(\mathbf{X}_i) = 0$ for all $\mathbf{X}_i \in \partial\Omega_u$ (Nguyen-Thanh et al., 2020). Alternatively, $A_i(\mathbf{x})$ and $B_i(\mathbf{x})$ can be pre-trained NNs that satisfy the BCs (Rao et al., 2021).

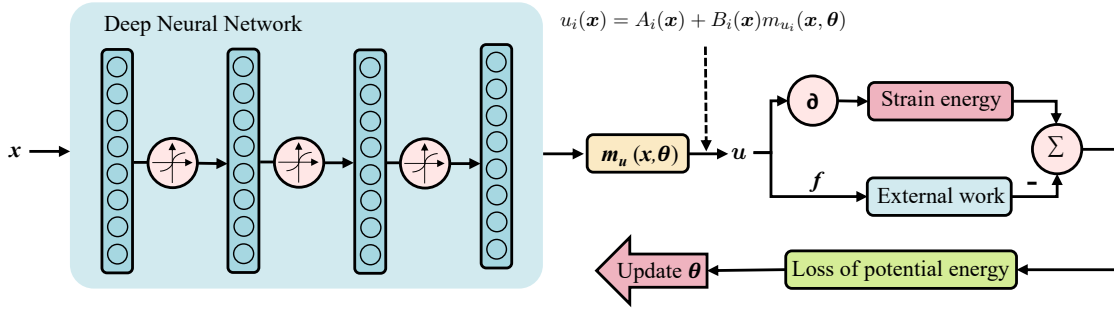


Fig. 1 Deep energy method: The displacement field is obtained by minimizing the total potential functional in Equation (7). Kinematic admissibility in this architecture is ensured via Equation (8).

3 Proposed Framework

TO determines the spatial material distribution that minimizes the scalar objective functional $L_C(\mathbf{u}(\mathbf{x}, \rho), \rho(\mathbf{x}))$ subject to a set of design constraints $C_i(\rho(\mathbf{x})) = 0$ for $i = 1, \dots, n_c$. We presume that the constraints imposed by the BCs are described by $R_b^{(i)}(\mathbf{u}(\mathbf{x}, \rho))$ and that the underlying physics of the system are governed by a set of state equations $R_p^{(i)}(\mathbf{u}(\mathbf{x}, \rho), \rho(\mathbf{x}))$ where $\mathbf{u}(\mathbf{x}, \rho) = [u_1(\mathbf{x}, \rho), u_2(\mathbf{x}, \rho)]^T$ denotes the two displacement components which are functions of the spatial coordinate $\mathbf{x} = [x, y]^T$ and the design variable $\rho(\mathbf{x})$. The general formulation of TO for CM can be written as:

$$\mathbf{u}(\mathbf{x}, \rho), \rho(\mathbf{x}) = \underset{\mathbf{u}, \rho}{\operatorname{argmin}} L_C(\mathbf{u}(\mathbf{x}, \rho), \rho(\mathbf{x})) = \underset{\mathbf{u}, \rho}{\operatorname{argmin}} \int_{\Omega} l_c(\mathbf{u}(\mathbf{x}, \rho), \rho(\mathbf{x})) dV, \quad (9a)$$

subject to:

$$C_1(\rho(\mathbf{x})) = \int_{\Omega} \rho(\mathbf{x}) dV - \psi_f V = 0, \quad (9b)$$

$$C_i(\rho(\mathbf{x})) = \int_{\Omega} c_i(\rho(\mathbf{x})) dV = 0, \quad i = 2, \dots, n_c, \quad (9c)$$

$$R_p^{(i)}(\mathbf{u}(\mathbf{x}, \rho), \rho(\mathbf{x})) = \int_{\Omega} r_p^{(i)}(\mathbf{u}(\mathbf{x}, \rho), \rho(\mathbf{x})) dV = 0, \quad i = 1, 2, \quad (9d)$$

$$R_b^{(i)}(\mathbf{u}(\mathbf{x}, \rho)) = \int_{\partial\Omega_u} r_b^{(i)}(\mathbf{u}(\mathbf{x}, \rho)) dA = 0, \quad i = 1, \dots, n_b, \quad (9e)$$

$$\rho(\mathbf{x}) \in [0, 1], \quad \forall \mathbf{x} \in \Omega, \quad (9f)$$

where V is the domain volume and ψ_f is the target volume fraction, the residuals $R_p^{(i)}(\mathbf{u}(\mathbf{x}, \rho), \rho(\mathbf{x}))$ and $R_b^{(i)}(\mathbf{u}(\mathbf{x}, \rho))$ correspond to PDEs and BCs/ICs, respectively. Equation (9) assumes that the objective function, constraints, and residuals can be represented as integrals of appropriately defined local functions.

We construct our PIGP framework based on the DEM method where the potential energy is minimized instead of the PDE residuals. Accordingly, for CM of linear elastic solids, we replace Equation (9d) with the potential energy functional $L_P(\mathbf{u}(\mathbf{x}, \rho), \rho(\mathbf{x}))$:

$$\mathbf{u}(\mathbf{x}, \rho), \rho(\mathbf{x}) = \underset{\mathbf{u}, \rho}{\operatorname{argmin}} L_C(\mathbf{u}(\mathbf{x}, \rho), \rho(\mathbf{x})) = \underset{\mathbf{u}, \rho}{\operatorname{argmin}} \int_{\Omega} l_c(\mathbf{u}(\mathbf{x}, \rho), \rho(\mathbf{x})) dV, \quad (10a)$$

subject to:

$$\begin{aligned} \mathbf{u}(\mathbf{x}, \rho) &= \underset{\mathbf{u}}{\operatorname{argmin}} L_P(\mathbf{u}(\mathbf{x}, \rho), \rho(\mathbf{x})) \\ &= \underset{\mathbf{u}}{\operatorname{argmin}} \left(\frac{1}{2} \int_{\Omega} l_p(\mathbf{u}(\mathbf{x}, \rho), \rho(\mathbf{x})) dV - \int_{\partial\Omega_F} \mathbf{f}(\mathbf{x})^T \mathbf{u}(\mathbf{x}, \rho) dA \right), \end{aligned} \quad (10b)$$

$$C_1(\rho(\mathbf{x})) = \int_{\Omega} \rho(\mathbf{x}) dV - \psi_f V = 0, \quad (10c)$$

$$C_i(\rho(\mathbf{x})) = \int_{\Omega} c_i(\rho(\mathbf{x})) dV = 0, \quad i = 2, \dots, n_c, \quad (10d)$$

$$R_b^{(i)}(\mathbf{u}(\mathbf{x}, \rho)) = \int_{\partial\Omega_u} r_b^{(i)}(\mathbf{u}(\mathbf{x}, \rho)) dA = 0, \quad i = 1, \dots, n_b, \quad (10e)$$

$$\rho(\mathbf{x}) \in [0, 1], \quad \forall \mathbf{x} \in \Omega, \quad (10f)$$

where $l_p(\mathbf{u}, \rho)$ is the strain energy density function. To solve the constrained optimization problem in Equation (10) with a simultaneous and mesh-free approach, we first parameterize all variables via the differentiable multi-output function $\mathbf{z}(\mathbf{x}; \boldsymbol{\zeta})$:

$$\mathbf{z}(\mathbf{x}; \boldsymbol{\zeta}) := [u_1(\mathbf{x}, \rho), u_2(\mathbf{x}, \rho), \rho(\mathbf{x})]^T, \quad (11)$$

where $\boldsymbol{\zeta}$ denotes the parameters. Then, we reformulate the constrained problem in Equation (10) as the unconstrained optimization problem using the penalty method (Nocedal and Wright, 2006):

$$\begin{aligned} \boldsymbol{\zeta} = \underset{\boldsymbol{\zeta}}{\operatorname{argmin}} L(\mathbf{z}(\mathbf{x}; \boldsymbol{\zeta})) &= \underset{\boldsymbol{\zeta}}{\operatorname{argmin}} \left[L_C(\mathbf{z}(\mathbf{x}; \boldsymbol{\zeta})) + \alpha_0 L_P(\mathbf{z}(\mathbf{x}; \boldsymbol{\zeta})) + \alpha_1 C_1^2(\mathbf{z}(\mathbf{x}; \boldsymbol{\zeta})) + \right. \\ &\quad \left. \sum_{i=2}^{n_c} \alpha_i C_i^2(\mathbf{z}(\mathbf{x}; \boldsymbol{\zeta})) + \sum_{j=1}^{n_b} \alpha_j R_b^{(j)}(\mathbf{z}(\mathbf{x}; \boldsymbol{\zeta}))^2 \right], \end{aligned} \quad (12)$$

where α_i for $i = 0, 1, \dots, n_b + n_c$ are scalar penalty factors, and for notational convenience the shorthands $z_\rho(\mathbf{x}; \boldsymbol{\zeta}) := \rho(\mathbf{x})$ and $\mathbf{z}_u(\mathbf{x}; \boldsymbol{\zeta}) := [u_1(\mathbf{x}, \rho), u_2(\mathbf{x}, \rho)]^T$ are defined. As detailed below, each term on the right-hand side of Equation (12) can be evaluated by numerically approximating the integrals.

When parameterizing the solution space, we represent both $\mathbf{u}(\mathbf{x}, \rho)$ and $\rho(\mathbf{x})$ as outputs of a single function, i.e., $\mathbf{z}(\mathbf{x}; \boldsymbol{\zeta})$, to capture their natural correlations. However, this unified formulation must (1) be sufficiently expressive to capture diverse topologies and their associated state fields, (2) be able to capture sharp interfaces and stress localizations and (3) accommodate efficient gradient computation with respect to both $\boldsymbol{\zeta}$ and \mathbf{x} , particularly for estimating the gradient of the objective function in Equation (12) with respect to $\rho(\mathbf{x})$ at each CP using the adjoint Lagrangian method. In the following subsections, we introduce a specific ML-based parametrization that not only has the above features, but also simplifies the optimization process.

3.1 Parameterization of State and Design Variables

While a gradient-based optimizer can solve the minimization problem in Equation (12), care must be taken to ensure all the terms on the right-hand side are effectively minimized within a reasonable number of optimization iterations. This is especially important because the scale of the various terms in Equation (12) can dramatically change during the optimization. Moreover, we have observed that if the BCs are not strictly enforced during the entire optimization process, the estimated solution fields (i.e., the displacements) and hence the designed topology substantially suffer. To address all of these issues, we introduce a particular form for $\mathbf{z}(\mathbf{x}; \boldsymbol{\zeta})$.

Specifically, we place GP priors on all state and design variables to leverage their reproducing property which, as shown below, allows the exclusion of all data-based constraints (e.g., BC residuals or specific design constraints) from Equation (12). These GP priors are equipped with distinct kernels but share a common multi-output mean function. We denote this mean function, parameterized by $\boldsymbol{\theta}$, as:

$$\mathbf{m}(\mathbf{x}; \boldsymbol{\theta}) = [m_{u_1}(\mathbf{x}; \boldsymbol{\theta}), m_{u_2}(\mathbf{x}; \boldsymbol{\theta}), m_\rho(\mathbf{x}; \boldsymbol{\theta})]^T, \quad (13)$$

where $m_{u_1}(\mathbf{x}; \boldsymbol{\theta})$, $m_{u_2}(\mathbf{x}; \boldsymbol{\theta})$, and $m_\rho(\mathbf{x}; \boldsymbol{\theta})$ denote the mean functions for the two displacement components and the density, respectively. The parametric form of this shared mean function will be discussed in detail in Section 3.1.1. To illustrate the reproducing property of GPs for the displacement variables, we express the posterior distribution of a GP prior conditioned on the prescribed displacements as:

$$u_i(\mathbf{x}^*; \boldsymbol{\theta}, \phi_{u_i}) := \mathbb{E}[u_i^* | \tilde{\mathbf{u}}_i, \mathbf{X}_i] = m_{u_i}(\mathbf{x}^*; \boldsymbol{\theta}) + \mathbf{V}_i^T \mathbf{r}_i, \quad (14a)$$

$$\mathbf{V}_i = c_i^{-1}(\mathbf{X}_i, \mathbf{X}_i; \phi_{u_i}) c_i(\mathbf{X}_i, \mathbf{x}^*; \phi_{u_i}), \quad (14b)$$

$$\mathbf{r}_i = \tilde{\mathbf{u}}_i - m_{u_i}(\mathbf{X}_i; \boldsymbol{\theta}), \quad (14c)$$

where $i = 1, 2$ corresponds to the two spatial dimensions, $\mathbf{x}^* = [x^*, y^*]^T$ is an arbitrary query point in the design domain, and $c_i(\mathbf{x}, \mathbf{x}'; \phi_{u_i})$ denotes the kernel with hyper-parameters ϕ_{u_i} . The vector $\tilde{\mathbf{u}}_i$ represents the prescribed displacements at points \mathbf{X}_i and so the *residual* vector \mathbf{r}_i quantifies the error of $m_{u_i}(\mathbf{X}; \boldsymbol{\theta})$ in matching $\tilde{\mathbf{u}}_i$. Using \mathbf{X}_i in place of \mathbf{x}^* it can be easily verified that the left-hand side of Equation (14a) equals $\tilde{\mathbf{u}}_i$ regardless of the choice of the mean function and the kernel. Hence, we can sample from the functions that specify the constraints on the state variables and then use those samples in our parameterization to automatically ensure that it always satisfies the BC constraints (as long as sufficient samples are taken from the constraint functions).

Similar to Equation (14) we parametrize the intermediate density field as:

$$\rho(\mathbf{x}^*; \boldsymbol{\theta}, \phi_\rho) := \mathbb{E}[\rho^* | \tilde{\boldsymbol{\rho}}, \mathbf{X}_\rho] = m_\rho(\mathbf{x}^*; \boldsymbol{\theta}) + \mathbf{V}_\rho^T \mathbf{r}_\rho, \quad (15a)$$

$$\mathbf{V}_\rho = c_\rho^{-1}(\mathbf{X}_\rho, \mathbf{X}_\rho; \phi_\rho) c_\rho(\mathbf{X}_\rho, \mathbf{x}^*; \phi_\rho), \quad (15b)$$

$$\mathbf{r}_\rho = \tilde{\boldsymbol{\rho}} - m_\rho(\mathbf{X}_\rho; \boldsymbol{\theta}), \quad (15c)$$

where the vector $\tilde{\boldsymbol{\rho}}$ is the prescribed design variables at points \mathbf{X}_ρ . Now, to constrain $\rho(\mathbf{x}; \boldsymbol{\theta}, \phi_\rho)$ to the admissible range $[0, 1]$ and promote binary separation for the final density function $\rho(\mathbf{x}; \boldsymbol{\theta}, \phi_\rho)$, the projection function $P(\cdot)$ (Wang et al., 2011) is applied to the parametrization in Equation (15) as:

$$P(\rho(\mathbf{x}; \boldsymbol{\theta}, \phi_\rho)) = \frac{\tanh(\beta \rho_t) + \tanh(\beta(\rho(\mathbf{x}; \boldsymbol{\theta}, \phi_\rho) - \rho_t))}{\tanh(\beta \rho_t) + \tanh(\beta(1 - \rho_t))}, \quad (16)$$

where $\rho_t = 0.5$ is the threshold density and $\beta = 8$ controls the sharpness of the transition between the two phases. Using the parameterizations in Equation (14) and Equation (16), we redefine the parameterization in Equation (11) as:

$$\mathbf{z}'(\mathbf{x}; \boldsymbol{\theta}, \phi) := [u_1(\mathbf{x}; \boldsymbol{\theta}, \phi_{u_1}), u_2(\mathbf{x}; \boldsymbol{\theta}, \phi_{u_2}), \rho(\mathbf{x}; \boldsymbol{\theta}, \phi_\rho)]^T, \quad (17)$$

where $\mathbf{z}'_u(\mathbf{x}; \boldsymbol{\theta}, \phi_u) := \mathbf{u}(\mathbf{x}; \boldsymbol{\theta}, \phi_u) = [u_1(\mathbf{x}; \boldsymbol{\theta}, \phi_{u_1}), u_2(\mathbf{x}; \boldsymbol{\theta}, \phi_{u_2})]^T$, $\mathbf{z}'_\rho(\mathbf{x}; \boldsymbol{\theta}, \phi_\rho) := \rho(\mathbf{x}; \boldsymbol{\theta}, \phi_\rho)$, $\phi = [\phi_{u_1}, \phi_{u_2}, \phi_\rho]$, and $\phi_u = [\phi_{u_1}, \phi_{u_2}]$.

The performance of our parameterization depends on the kernels chosen for each variable. For simplicity and computational efficiency, we follow the recommendations of Mora et al. (2024) and use the Gaussian kernel for all of our variables:

$$c(\mathbf{x}, \mathbf{x}'; \phi) = s^2 \exp\{-(\mathbf{x} - \mathbf{x}')^T \text{diag}(\phi) (\mathbf{x} - \mathbf{x}')\} + \mathbb{1}\{\mathbf{x} == \mathbf{x}'\} \delta, \quad (18)$$

where $\mathbb{1}$ is a binary indicator function that returns 1 when $\mathbf{x} == \mathbf{x}'$ and 0 otherwise, s^2 denotes the process variance, and $\delta = 10^{-5}$ is the nugget (a small positive number) that ensures the invertibility of the covariance matrix $c(\mathbf{X}, \mathbf{X}; \phi)$. As recommended by Mora et al. (2024), we assign independent kernels with *fixed* hyperparameters to each mean function in Equation (13) to make sure the state and design variables strictly satisfy the applied constraints. The rationale for using separate kernels is as follows: (1) it facilitates the handling of heterogeneous data, particularly when BCs for state variables and prescribed design features are defined at different locations or along complex geometries; (2) it reduces computational and memory costs by allowing independent covariance matrices to be constructed for each output variable, rather than a single large joint matrix. Additionally, fixing ϕ allows us to pre-compute, invert, and cache all covariance matrices; dramatically decreasing the training costs while ensuring numerical stability. Compared with our previous work (Yousefpour et al., 2025), we heuristically select² a relatively small length-scale parameter $\phi = 0.5$ for all kernels and keep it fixed throughout training.

Using Equation (17) with fixed $\hat{\phi}$, we now rewrite Equation (12) as:

$$\begin{aligned} \hat{\boldsymbol{\theta}} = \underset{\boldsymbol{\theta}}{\text{argmin}} L(\mathbf{z}'(\mathbf{x}; \boldsymbol{\theta}, \hat{\phi})) &= \underset{\boldsymbol{\theta}}{\text{argmin}} \left[L_C(\mathbf{z}'(\mathbf{x}; \boldsymbol{\theta}, \hat{\phi})) + \alpha_0 L_P(\mathbf{z}'(\mathbf{x}; \boldsymbol{\theta}, \hat{\phi})) \right. \\ &\quad \left. + \alpha_1 C_1^2(\mathbf{z}'_\rho(\mathbf{x}; \boldsymbol{\theta}, \hat{\phi}_\rho)) \right] \end{aligned} \quad (19)$$

where all data-based design constraints (except the one on volume fraction) are dropped due to the reproducing property of our parametrization with GPs.

²Further details on the heuristic selection of ϕ are provided in Appendix C.

It is important to highlight that Equation (17) is fundamentally different from Equation (11) since our parameterizations in Equations (14) and (15) do *not* explicitly capture the underlying dependency of displacements on the density. As detailed in Section 3.2, we implicitly build this dependency into our framework by reformulating the gradients that are used by the Adam optimizer.

3.1.1 Shared Mean Function

As motivated earlier, we use a specific NN architecture as the shared mean function of all the three GPs in Equations (14) and (15). Specifically, we use PGCAN which we have recently developed (Shishehbor et al., 2024) to address the spectral bias of MLPs: The idea behind PGCAN is to represent the spatiotemporal domain with a grid-based parametric encoder that has learnable features on its vertices. The encoder is followed by a decoder (an MLP with attention layers) to convert the features to the outputs (displacements and density in our case). For any query point in the domain, its feature vector is obtained by interpolating the feature vectors of the vertices of its enclosing cell³. That is, the model’s predictions at \mathbf{x} do *not* depend on all the features of the encoder; rather they only depend on the features of the cell that encloses \mathbf{x} . This property enables PGCAN to mitigate spectral bias and more accurately estimate high-gradient solutions.

Shishehbor et al. (2024) demonstrate that a grid-based encoder is susceptible to overfitting and to mitigate this issue, we (1) convolve the features with a small kernel, and (2) have multiple grids which are diagonally shifted with respect to the original one so that a query point’s coordinates are slightly perturbed. So, as schematically illustrated in Fig. 2 for a 2D spatial domain, our PGCAN parametrizes the domain via the trainable feature tensor $\mathbf{F}_0 \in \mathbb{R}^{N_{rep} \times N_f \times N_x^e \times N_y^e}$ where N_{rep} denotes the number of grid repetitions, $N_f = 128$ represents the number of features per grid vertex, and N_x^e and N_y^e specify the number of vertices along the x and y directions, respectively. To promote information flow across neighboring cells, we apply a 3×3 convolution with N_f input and output channels to \mathbf{F}_0 followed by a tanh activation function. The resulting feature map $\mathbf{F}_c \in \mathbb{R}^{N_{rep} \times N_f \times N_x^e \times N_y^e}$ is placed over the spatial domain with N_{rep} small diagonal offsets ($N_{rep} = 3$ in Fig. 2).

To compute the feature vector at the arbitrary query point \mathbf{x} , we first obtain the local (i.e., within cell) coordinates $\bar{\mathbf{x}} \in [0, 1]$ and then apply cosine transformation to them to enable differentiability with respect to the inputs:

$$\mathbf{x}^* = \frac{1}{2}(1 - \cos(\pi\bar{\mathbf{x}})). \quad (20)$$

Then, the feature vector at $\mathbf{x}^* = [x^*, y^*]^T$ corresponding to each grid $m \in \{1, \dots, N_{rep}\}$ with perturbation is obtained by bilinearly interpolating the features at the vertices of the cell that encloses \mathbf{x}^* :

$$\mathbf{f}_t^m(\mathbf{x}^*) = (1 - x^*)(1 - y^*)\mathbf{f}_{t(0,0)}^m + (1 - x^*)y^*\mathbf{f}_{t(0,1)}^m + x^*(1 - y^*)\mathbf{f}_{t(1,0)}^m + x^*y^*\mathbf{f}_{t(1,1)}^m, \quad (21)$$

where $\mathbf{f}_{t(i,j)}^m \in \mathbb{R}^{N_f}$ with $i, j \in \{0, 1\}$ are the extracted features from \mathbf{F}_c . The final feature vector at the query point is obtained by summing the feature vectors across the grid repetitions, i.e., $\mathbf{f}_t(\mathbf{x}) = \sum_m \mathbf{f}_t^m(\mathbf{x}^*)$.

Once $\mathbf{f}_t(\mathbf{x})$ is obtained, it is split into two vectors of equal length $\mathbf{f}_{t_1}(\mathbf{x})$ and $\mathbf{f}_{t_2}(\mathbf{x})$ and passed to a shallow decoder network with 3 hidden layers of 64 neurons. As described in Shishehbor et al. (2024), these features are used to sequentially modulate the hidden states of the network, thereby enhancing gradient propagation during training.

³Note that the encoder partitions the input space into cells but this does *not* translate into any discretization due to the fact that we can obtain features for any point in the domain and then pass these features into the decoder to obtain the responses.

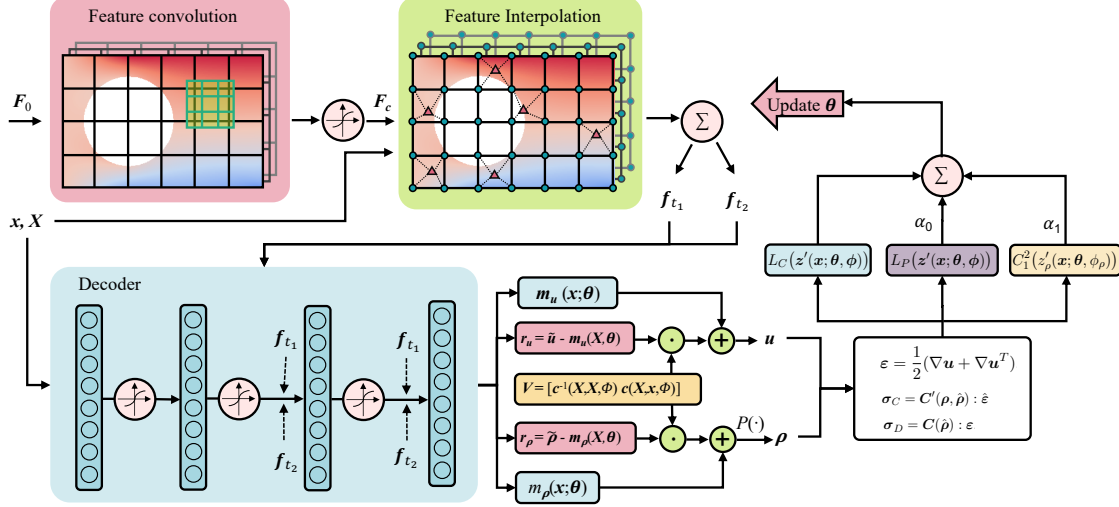


Fig. 2 PIGP framework for CM: the mean functions are parameterized with the multi-outputs from the PGCAN having three modules: convolutional neural network-based feature encoding, feature interpolation, and decoding via a shallow MLP. GPs are employed on those mean functions to impose displacement BCs and density constraints.

3.2 Physics-based Gradients

While $\partial L(\cdot)/\partial \theta$ can be readily obtained based on Equation (19) using AD, it cannot be directly used to optimize θ because of the following reasons. First, the penalty term corresponding to the total potential energy can become negative during the optimization. So, we must augment $L_P(\cdot)$ with a term that ensures $L_P(\cdot)$ remains positive during the optimization (otherwise it cannot serve as a proper regularizer). Second, our parameterization does not explicitly make $u(\cdot)$ dependent on $\rho(\cdot)$ which is a physical requirement. Introducing this dependence relies on deriving the gradients of $L_C(\cdot)$ and $L_P(\cdot)$ based on the physics of the problem such that they can be added and then used for updating θ at each optimization iteration.

Referring to Section 2 we observe that the displacement field is obtained by minimizing the total potential of a fixed system, i.e., the minimization must be done for a fixed $\rho(\cdot)$. So, there must be no contributions from the density to the gradients, i.e., $\partial L_P(\cdot)/\partial \theta = \frac{\partial L_P}{\partial u} \frac{\partial u}{\partial \theta} + 0$ where $\frac{\partial L_P}{\partial \rho} \frac{\partial \rho}{\partial \theta}$ is replaced by 0. Conversely, for the compliance, the gradients are taken with respect to the density field while the displacement (or strain⁴) field is fixed *and* assumed to satisfy the force equilibrium constraints. As detailed below, we satisfy these conditions by obtaining $\partial L_C(\cdot)/\partial \rho(\cdot)$ based on the adjoint method.

To accommodate the above requirements we remove or detach the gradients with respect to certain variables in our computational graph. To facilitate the descriptions, we denote *detached* variables with a hat symbol such as $\hat{\varepsilon}(x; \theta, \phi_u)$ and $\hat{\rho}(x; \theta, \phi)$ which do not have gradients and share the same numerical values as their with-gradient counterparts. Using these detached variables, the individual terms in Equation (19)

⁴While fixing the strains or displacements provide the same results, we choose the former due to its computational efficiency.

can be approximated as:

$$L_C(z'(x; \theta, \phi)) = \frac{V}{n_{cp}} \sum_{i=1}^{n_{cp}} \sigma_C(x_i; \theta, \phi) : \hat{\varepsilon}(x_i; \theta, \phi_u), \quad (22a)$$

$$L_P(z'(x; \theta, \phi)) = \frac{V}{2n_{cp}} \sum_{i=1}^{n_{cp}} \sigma_P(x_i; \theta, \phi) : \varepsilon(x_i; \theta, \phi_u) - \sum_{i=1}^{n_f} \mathbf{f}(x_i)^T \mathbf{u}(x_i; \theta, \phi_u) s_i + \tau(z'(x; \theta, \phi)), \quad (22b)$$

$$C_1^2(z'_\rho(x; \theta, \phi_\rho)) = \left(\frac{1}{n_{cp}} \sum_{i=1}^{n_{cp}} \rho(x_i; \theta, \phi_\rho) / \psi_f - 1 \right)^2, \quad (22c)$$

where n_{cp} and n_f denote the numbers of CPs in the entire domain and along the traction BCs, respectively. The offset term $\tau(\cdot)$ as well as the two stress tensors $\sigma_C(\cdot)$ and $\sigma_P(\cdot)$ are calculated as detailed below.

At force equilibrium, $L_P(\cdot)$ is negative since the strain energy equals one half of the external work. Even before equilibrium during training, a specific set of parameters might cause $L_P(\cdot)$ to become negative. Since a negative $L_P(\cdot)$ cannot be a regularizer, we add $\tau(\cdot)$ to it:

$$\tau(z'(x; \theta, \phi)) := \frac{\Delta}{2} \sum_{i=1}^{n_f} \mathbf{f}(x_i)^T \hat{\mathbf{u}}(x_i; \theta, \phi_u) s_i, \quad (23)$$

where $\Delta = 1.01$ is a constant that is slightly greater than 1 to ensure that $\tau(\cdot)$ is always greater than one half of the external work (which has a negative sign in $L_P(\cdot)$, see Equation (7)). Note that $\tau(\cdot)$ is based on $\hat{\mathbf{u}}(\cdot)$ so it does not have any gradients with respect to $\mathbf{u}(\cdot)$.

The two stress tensors in Equation (22) are calculated via the constitutive law of a linear elastic material:

$$\sigma_C(x; \theta, \phi) := \mathbf{C}_C(x; \theta, \phi_\rho) : \hat{\varepsilon}(x; \theta, \phi_u), \quad (24a)$$

$$\sigma_P(x; \theta, \phi) := \mathbf{C}_P(x; \theta, \phi_\rho) : \varepsilon(x; \theta, \phi_u), \quad (24b)$$

where both $\mathbf{C}_C(\cdot)$ and $\mathbf{C}_P(\cdot)$ are stiffness tensors that are numerically the same but have different gradients. We achieve this feature by appropriately parameterizing the Young's modulus which, in turn, affects the gradients of stiffness tensor with respect to $\rho(\cdot)$. Following the SIMP methodology, we build $\mathbf{C}_P(\cdot)$ based on the following Young's modulus:

$$E_P(x; \theta, \phi_\rho) = E_{min} + \hat{\rho}^p(x; \theta, \phi_\rho)(E_{max} - E_{min}), \quad (25)$$

where $E_{max} = 1$ denotes the Young's modulus of the solid phase, $E_{min} = 10^{-3}$ is a small positive constant introduced to further ensure numerical stability, and $p = 3$ is a penalty factor that promotes binary designs. The Poisson's ratio ν is fixed at 0.3 to construct stiffness tensors.

In Section 3.2.1 we use the adjoint variable method to demonstrate that $\mathbf{C}_C(\cdot)$ can be constructed via the following Young's modulus:

$$E_C(x; \theta, \phi_\rho) = E_{min} + \frac{\hat{\rho}^{2p}(x; \theta, \phi_\rho)}{\hat{\rho}^p(x; \theta, \phi_\rho) + \epsilon} (E_{max} - E_{min}), \quad (26)$$

which has the same numerical value as in Equation (25) but has different gradients, and $\epsilon = 10^{-5}$ is a small constant introduced to ensure numerical stability. It is straightforward to verify that, using Equation (26), the gradient of $L_C(z'(x; \theta, \phi))$ with respect to $\rho(x; \theta, \phi_\rho)$ reproduces the same gradient as given in Equation (33) from the adjoint variable method.

3.2.1 Sensitivity Analysis by Adjoint Variable Method

We use the adjoint method to obtain the gradient of $L_C(\cdot)$ with respect to $\rho(\cdot)$ while (1) detaching the gradients with respect to $\mathbf{u}(\cdot)$ as motivated earlier, and (2) consider the dependence of $\mathbf{u}(\cdot)$ on $\rho(\cdot)$ based on the physics of the problem. We start by writing the Lagrangian:

$$\begin{aligned} L_C(\mathbf{u}(\mathbf{x}, \rho), \rho(\mathbf{x}), \boldsymbol{\lambda}(\mathbf{x})) &= \int_{\Omega} l_c(\mathbf{u}(\mathbf{x}, \rho), \rho(\mathbf{x})) dV + \int_{\Omega} \boldsymbol{\lambda}^T(\mathbf{x}) (\nabla \cdot \boldsymbol{\sigma}(\mathbf{x})) dV \\ &= \int_{\Omega} \boldsymbol{\varepsilon}(\mathbf{x}) : \mathbf{C}(\mathbf{x}) : \boldsymbol{\varepsilon}(\mathbf{x}) dV + \int_{\Omega} \boldsymbol{\lambda}^T(\mathbf{x}) (\nabla \cdot \boldsymbol{\sigma}(\mathbf{x})) dV, \end{aligned} \quad (27)$$

where $\boldsymbol{\lambda}(\mathbf{x}) = [\lambda_1(\mathbf{x}), \lambda_2(\mathbf{x})]^T$ are the Lagrange multipliers. Using the divergence theorem, the last term on the right-hand side of Equation (27) can be expanded as:

$$\int_{\Omega} \boldsymbol{\lambda}^T(\mathbf{x}) (\nabla \cdot \boldsymbol{\sigma}(\mathbf{x})) dV = - \int_{\Omega} \nabla \boldsymbol{\lambda}(\mathbf{x}) : \boldsymbol{\sigma}(\mathbf{x}) dV + \int_{\partial\Omega} \boldsymbol{\lambda}^T(\mathbf{x}) (\boldsymbol{\sigma}(\mathbf{x}) \mathbf{n}(\mathbf{x})) dA, \quad (28)$$

where $\mathbf{n}(\mathbf{x})$ denotes the outward unit normal vector on the domain boundary. Additionally, $\boldsymbol{\sigma}(\mathbf{x}) \mathbf{n}(\mathbf{x}) = \mathbf{f}(\mathbf{x})$ and since the Cauchy stress tensor $\boldsymbol{\sigma}(\mathbf{x})$ is symmetric, we have $\nabla \boldsymbol{\lambda}(\mathbf{x}) : \boldsymbol{\sigma}(\mathbf{x}) = \text{sym}(\nabla \boldsymbol{\lambda}(\mathbf{x})) : \boldsymbol{\sigma}(\mathbf{x}) = \boldsymbol{\varepsilon}_{\boldsymbol{\lambda}}(\mathbf{x}) : \boldsymbol{\sigma}(\mathbf{x})$ where $\boldsymbol{\varepsilon}_{\boldsymbol{\lambda}}(\mathbf{x})$ denotes the strain tensor associated with the augmented field $\boldsymbol{\lambda}(\mathbf{x})$. So, we can rewrite Equation (27) as:

$$L_C(\cdot) = \int_{\Omega} \boldsymbol{\varepsilon}(\mathbf{x}) : \mathbf{C}(\mathbf{x}) : \boldsymbol{\varepsilon}(\mathbf{x}) dV - \int_{\Omega} \boldsymbol{\varepsilon}_{\boldsymbol{\lambda}}(\mathbf{x}) : \mathbf{C}(\mathbf{x}) : \boldsymbol{\varepsilon}(\mathbf{x}) dV + \int_{\partial\Omega} \boldsymbol{\lambda}(\mathbf{x})^T \mathbf{f}(\mathbf{x}) dA. \quad (29)$$

Assuming that the external force $\mathbf{f}(\mathbf{x})$ is independent of $\rho(\mathbf{x})$, the total derivative of $L_C(\cdot)$ with respect to $\rho(\cdot)$ is given as:

$$\begin{aligned} \frac{dL_C(\cdot)}{d\rho} &= 2 \int_{\Omega} \left(\frac{\partial \boldsymbol{\varepsilon}(\mathbf{x})}{\partial \mathbf{u}} : \frac{\partial \mathbf{u}}{\partial \rho} \right) : \mathbf{C}(\mathbf{x}) : \boldsymbol{\varepsilon}(\mathbf{x}) dV + \int_{\Omega} \boldsymbol{\varepsilon}(\mathbf{x}) : \frac{\partial \mathbf{C}(\mathbf{x})}{\partial \rho} : \boldsymbol{\varepsilon}(\mathbf{x}) dV \\ &\quad - \int_{\Omega} \boldsymbol{\varepsilon}_{\boldsymbol{\lambda}}(\mathbf{x}) : \frac{\partial \mathbf{C}(\mathbf{x})}{\partial \rho} : \boldsymbol{\varepsilon}(\mathbf{x}) dV - \int_{\Omega} \boldsymbol{\varepsilon}_{\boldsymbol{\lambda}}(\mathbf{x}) : \mathbf{C}(\mathbf{x}) : \left(\frac{\partial \boldsymbol{\varepsilon}(\mathbf{x})}{\partial \mathbf{u}} : \frac{\partial \mathbf{u}}{\partial \rho} \right) dV, \end{aligned} \quad (30)$$

where we have used the fact that the stiffness tensor $\mathbf{C}(\mathbf{x})$ is symmetric, that is:

$$\int_{\Omega} \frac{\partial \boldsymbol{\varepsilon}(\mathbf{x})}{\partial \mathbf{u}} : \frac{\partial \mathbf{u}}{\partial \rho} : \mathbf{C}(\mathbf{x}) : \boldsymbol{\varepsilon}_{\boldsymbol{\lambda}}(\mathbf{x}) dV = \int_{\Omega} \boldsymbol{\varepsilon}_{\boldsymbol{\lambda}}(\mathbf{x}) : \mathbf{C}(\mathbf{x}) : \frac{\partial \boldsymbol{\varepsilon}(\mathbf{x})}{\partial \mathbf{u}} : \frac{\partial \mathbf{u}}{\partial \rho} dV. \quad (31)$$

Introducing $\mathbf{A}(\cdot) = \frac{\partial \boldsymbol{\varepsilon}(\mathbf{x})}{\partial \mathbf{u}} : \frac{\partial \mathbf{u}}{\partial \rho}$, we can write Equation (30) as:

$$\frac{dL_C(\cdot)}{d\rho} = \int_{\Omega} \mathbf{A}(\mathbf{x}) : \mathbf{C}(\mathbf{x}) : (2\boldsymbol{\varepsilon}(\mathbf{x}) - \boldsymbol{\varepsilon}_{\boldsymbol{\lambda}}(\mathbf{x})) dV + \int_{\Omega} (\boldsymbol{\varepsilon}(\mathbf{x}) - \boldsymbol{\varepsilon}_{\boldsymbol{\lambda}}(\mathbf{x})) : \frac{\partial \mathbf{C}(\mathbf{x})}{\partial \rho} : \boldsymbol{\varepsilon}(\mathbf{x}) dV. \quad (32)$$

Since the multiplier $\boldsymbol{\lambda}(\mathbf{x})$ is arbitrary, we set it such that $\boldsymbol{\varepsilon}_{\boldsymbol{\lambda}}(\mathbf{x}) = 2\boldsymbol{\varepsilon}(\mathbf{x})$ which simplifies Equation (32) to:

$$\frac{dL_C(\cdot)}{d\rho} = - \int_{\Omega} \boldsymbol{\varepsilon}(\mathbf{x}) : \frac{\partial \mathbf{C}(\mathbf{x})}{\partial \rho} : \boldsymbol{\varepsilon}(\mathbf{x}) dV, \quad (33)$$

where a negative sign appears in the gradient. So, in our approach, we define the Young's modulus per Equation (26) so that when AD is used to obtain the gradients, a negative sign appears.

3.3 Computational Accelerations and Stability

As mentioned earlier, in our implementation we assign a GP prior with fixed hyper-parameters to each variable. This choice dramatically accelerates the optimization process as covariance matrices and their inverses (see Equations (14) and (15)) can be pre-computed and stored for repeated uses while optimizing θ per Equation (19). To further increase the computational efficiency and robustness of our approach, we develop the following two strategies.

3.3.1 Numerical Approximations

We can improve computational performance by (1) numerically approximating some of the partial derivatives in Equation (22), and (2) arranging the CPs in particular configurations that accelerate convergence rate while reducing overfitting issues and memory requirements.

To simultaneously address these issues, we follow [Yousefpour et al. \(2025\)](#) who approximate the spatial derivatives such as $\partial \mathbf{u}(\cdot)/\partial \mathbf{x}$ via finite difference (FD). To this end, we place the CPs on a regular grid and pad the domain via two layers of points in each direction to increase gradient approximation accuracy close to the boundaries. This arrangement of CPs is in sharp contrast to most works where PDEs are solved via PIML because in these works the CPs are distributed in the domain either randomly or via a space-filling algorithm such as Sobol sequence. Details on our FD approximation and implementation are provided in Appendix B.

In addition to accelerating the estimation of spatial derivatives, arranging the CPs on a grid that does not change during optimization allows us to pre-compute and store the covariance matrices (and their inverses) that appear in Equations (14) and (15). This approach dramatically decreases the computational costs while increasing the robustness as repeated matrix inversion are eliminated.

The disadvantage of placing the CPs on a fixed regular grid is that, when combined with PGCAN, it can result into overfitting which is not observed in [Yousefpour et al. \(2025\)](#) as their work is based on MLPs. To address this issue, we define a series of grids with various resolutions and randomly select one for each optimization iteration. More specifically, we first define a fine and a coarse grid where the former is twice denser than the latter. Then, by linearly interpolating between these two grids, we generate a set of grids denoted by $\Sigma = [\mathbf{X}_1, \dots, \mathbf{X}_{n_g}]$ where \mathbf{X}_1 and \mathbf{X}_{n_g} represent the coarse and fine grids, respectively. For each grid in Σ , we pre-compute and cache relevant quantities such as CP coordinates and the corresponding external load vectors. During training, one grid is randomly sampled from Σ at each step and used to compute spatial gradients via FD and evaluate the loss function. Further details on the overfitting issue associated with a fixed grid and the impact of the proposed adaptive grid scheme are provided in Appendix D.

3.3.2 Curriculum Training

Our framework for CM aims to simultaneously minimize three loss terms. In our studies we have observed that when the target volume fraction is very low the training process can become unstable. This issue is manifested by the large oscillations in the loss histories and high roughness in the designed topologies.

Motivated by curriculum training, in which a model is progressively trained by adapting its learning objectives ([Soviany et al., 2022](#); [Yousefpour et al., 2025](#)), we address this issue by introducing a volume fraction scheduling strategy. In this strategy, we first initialize the target volume fraction ψ_f with a value of ψ_0 that is close to the average initial density predicted by the mean function. As training progresses, we linearly reduce this target volume fraction to the desired value ψ_l over a specified portion γ (e.g., 30% or

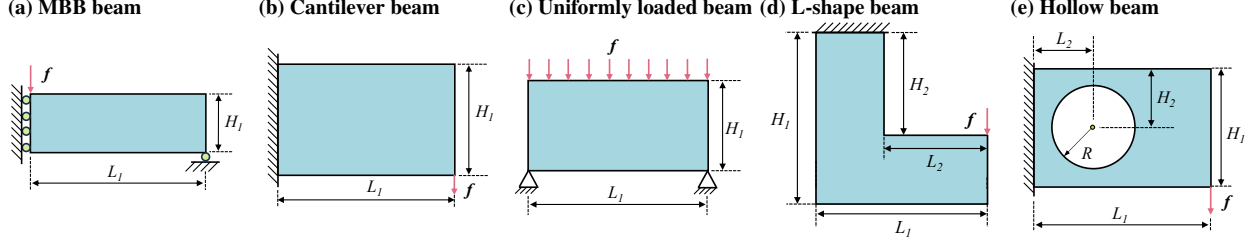


Fig. 3 Benchmark examples: We consider five cases for compliance minimization including (a) Messerschmitt-Bölkow-Blohm (MBB) beam, (b) Cantilever beam, (c) Uniformly loaded beam, (d) L-shape beam, and (e) Hollow beam with a circular hole.

50%) of the total training epochs. This strategy can be formulated as:

$$\psi_f = \begin{cases} \frac{\psi_l - \psi_0}{\gamma n_{tol}} n + \psi_0, & n \leq \gamma n_{tol}, \\ \psi_l, & n > \gamma n_{tol}, \end{cases} \quad (34)$$

where n_{tol} denotes the total number of epochs and γ controls the scheduling. The gradual reduction of volume fraction imposes a smooth topological evolution into the optimization; increasing the stability of the training. In all of our experiments we use $\psi_0 = 0.6$ and $\gamma = 50\%$.

4 Results and Discussion

We compare our approach against SIMP and other ML-based methods on a set of benchmarks. Specifically, we consider the five canonical examples illustrated in Fig. 3 with the corresponding dimensions, desired volume fractions, and applied external forces detailed in Table 1. The size of the design domains and magnitude of the loads are selected to satisfy the small deformation assumption of linear elasticity.

We implement SIMP in MATLAB and execute it on a Windows desktop with an Intel® Core™ i7-11700K CPU. Our PIGP framework is implemented in Python and executed on an NVIDIA A100 GPU. Due to the non-convex nature of TO, we run both approaches 10 times with different random initializations to assess variability. Three evaluation metrics are used for comparing the optimization effectiveness across the two approaches: final compliance, gray area fraction, and interface fraction. The final compliance is obtained via the FEM and the gray area is defined as the fraction of CPs (elements for SIMP) with density between 0.1 and 0.9. The interface fraction refers to the proportion of CPs or elements located on solid-void interfaces. More details about interface fraction are provided in Appendix E.

Table 1 Parameter values: Geometric parameters, external force, and target volume fractions for the five examples are listed. All dimensions are in mm and f denotes the external force magnitude for either a point (N) or distributed (N/mm) load.

Example	H_1 (mm)	L_1 (mm)	H_2 (mm)	L_2 (mm)	R (mm)	f (N or N/mm)	ψ_f
MBB beam	50	150	—	—	—	0.1	0.5
Cantilever beam	100	160	—	—	—	0.1	0.3
Uniformly Loaded beam	100	200	—	—	—	10^{-3}	0.3
L-shape beam	100	100	60	60	—	0.1	0.5
Hollow beam	100	150	50	50	33.33	0.1	0.5

As detailed in Section 3.3.1, we use the set of regular grids $\Sigma = [\mathbf{X}_1, \dots, \mathbf{X}_{n_g}]$ for estimating the loss components in Equation (19). Since the domain sizes in Fig. 3 are different, we ensure consistency by (1) selecting the coarse grid \mathbf{X}_1 such that the spacing between adjacent grid vertices is 1 mm along both H_1 and L_1 , and (2) density of grid cells in the fine grid \mathbf{X}_{n_g} is twice that of \mathbf{X}_1 . The CP resolutions of the coarse and fine grids, along with the corresponding n_g for each example, are summarized in Table 2. Our experiments indicate that the final topologies produced by our framework are insensitive to n_g , as long as it is set to a reasonably large constant (i.e., 100).

Table 2 Lowest and highest grid densities: The number of CPs $(N_x^{(1)}, N_y^{(1)})$ along L_1 and H_1 are enumerated for the coarse and fine grids in each example, along with the total number of grids n_g . The intermediate grids are constructed as detailed in Section 3.3.1.

Example	Coarse Grid $(N_x^{(1)}, N_y^{(1)})$	Fine Grid $(N_x^{(n_g)}, N_y^{(n_g)})$	n_g
MBB beam	(151, 51)	(301, 101)	150
Cantilever beam	(161, 101)	(321, 201)	160
Uniformly Loaded beam	(201, 101)	(401, 201)	200
L-shape beam	(101, 101)	(201, 201)	100
Hollow beam	(151, 101)	(301, 201)	150

We use PGCAN as the backbone network architecture across all benchmarks and include an MLP model for comparison. Both architectures use the swish activation function within the hidden layers. In PGCAN, we define N_x^e and N_y^e as the number of grid vertices along the x and y directions for the feature tensor $\mathbf{F}_0 \in \mathbb{R}^{N_{\text{rep}} \times N_f \times N_x^e \times N_y^e}$. N_x^e and N_y^e are determined using the resolution parameter Res, which specifies the number of grid vertices per 100mm edge length. Specifically,

$$N_x^e = \text{Res} \cdot \frac{L_1}{100}, \quad (35a)$$

$$N_y^e = \text{Res} \cdot \frac{H_1}{100}. \quad (35b)$$

In MLP, we use 6 fully-connected hidden layers with 64 neurons for each layer. We employ the Adam optimizer to train all models up to 20,000 epochs, with an initial learning rate of 10^{-3} that decays by a factor of 0.75 at four evenly spaced intervals. The loss weight factors in Equation (19) are fixed as $\alpha_0 = 10^2$ and $\alpha_1 = 10^3$ across all examples.

4.1 Comparison Studies and Topology Evolution

The comparison of the topological structures from our PIGP framework against those from SIMP is shown in Fig. 4. We employ the sensitivity filters (Sigmund, 2001) with radius 2 and 4 to address mesh-dependency while controlling the complexity of structures in SIMP. In our approach, we can control the structural complexity via Res and so consider two values (36 and 18) for it. The corresponding feature grids for all examples are displayed in Fig. 4 next to the obtained topologies by our method.

As shown in Fig. 4, the designed topologies by both approaches are quite similar in all cases. However, we observe that SIMP solutions tend to have higher gray fraction, especially when the filter size is set to 4. We also observe that both approaches can effectively control the complexity of the solutions by interpretable parameters (filter size in SIMP and number of cells in our approach’s PGCAN) where smaller filter

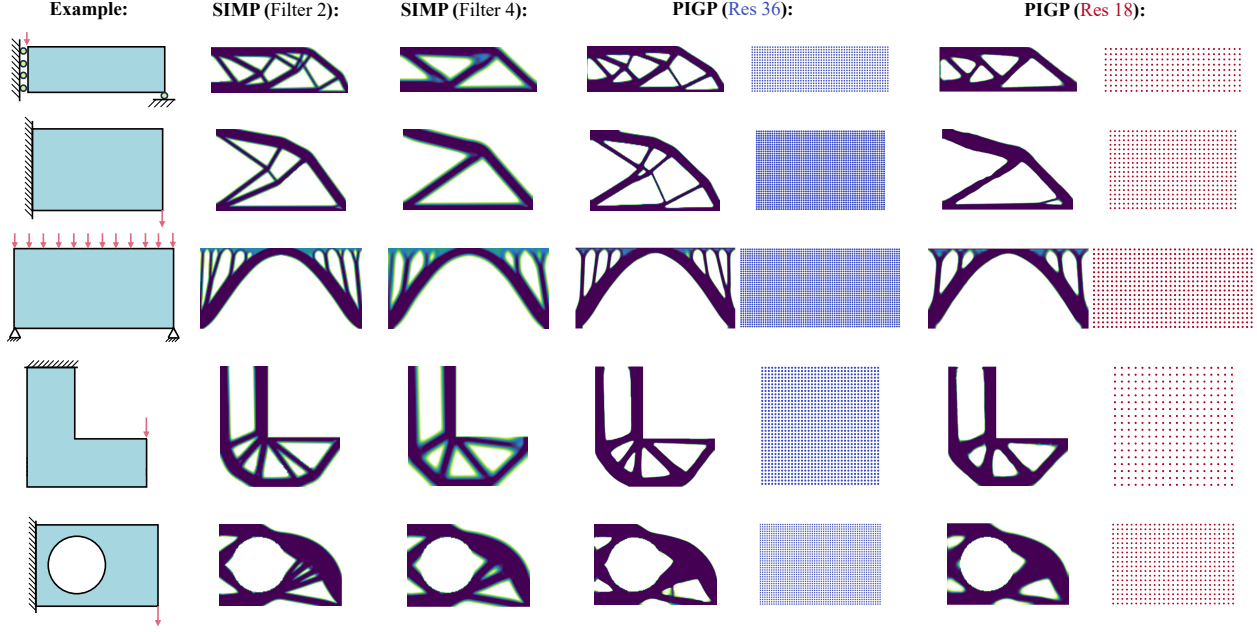


Fig. 4 Comparison of final designs: For both approaches we visualize the topologies corresponding to the median compliance in each example. The cell vertices of PGCAN are also shown to demonstrate the effect of Res on partitioning the design domain via PGCAN’s encoder.

radius and larger Res values result in more intricate designs. We will further examine the effects of Res in Section 4.3.

We report the median values of compliance (mJ), gray area fraction (%), and computation time (sec) in Table 3 across the 10 repetitions for each example using SIMP (Filter 2) and PIGP (Res 36) as comparison. Compliance values for both methods are computed using the FEM solver from (Andreassen et al., 2011). The median compliance values from our approach are consistently lower than those from SIMP for all examples. More importantly, our approach significantly outperforms SIMP in reducing gray area fractions, e.g., the median values for the cantilever beam are 2.3% vs 8.2%. However, our approach is slower than SIMP which leverages the self-adjoint nature of the problem to achieve significant speedups. Reducing computational costs is part of our future works.

Table 3 Summary of performance: Median values of compliance (mJ), gray area fraction (%), and computational time (sec) are listed for comparison between SIMP (Filter 2) and PIGP (Res 36). The reported computational time for PIGP corresponds to the total runtime over 20,000 training epochs.

Example	SIMP (Filter 2)			PIGP (Res 36)		
	Compliance	Gray Area	Time	Compliance	Gray Area	Time
MBB beam	2.048	14.9	7.5	1.999	5.4	549
Cantilever beam	0.774	8.2	15.3	0.758	2.3	765
Uniformly loaded beam	0.256	12.2	24.4	0.249	6.1	798
L-shape beam	2.013	9.6	8.4	1.837	3.1	609
Hollow beam	0.547	6.3	6.9	0.544	3.7	921

Statistical details of the compliance values for all five examples are summarized in Table 4. We observe that Our approach yields lower median and mean compliance values than SIMP, with the most notable difference corresponding to the L-shape beam example. The standard deviations in our results are slightly higher across most cases, indicating a greater design variability. Nevertheless, the relatively small standard deviations compared to the mean compliance values suggests that the randomness introduced by parameter initialization and our adaptive grid scheme is quite small.

Table 4 Statistical comparison of compliance: Median, mean, standard deviation, maximum, and minimum values for compliance (m.J) are reported for SIMP (Filter 2) and PIGP (Res 36).

Example	SIMP (Filter 2)					PIGP (Res 36)				
	median	mean	std	max	min	median	mean	std	max	min
MBB	2.048	2.05	1.3×10^{-2}	2.073	2.034	1.999	2.004	2.3×10^{-2}	2.053	1.979
Cantilever	0.774	0.778	7.6×10^{-3}	0.791	0.769	0.758	0.766	2.9×10^{-2}	0.844	0.747
Uniformly loaded	0.256	0.257	6.2×10^{-4}	0.258	0.255	0.249	0.249	1.6×10^{-3}	0.252	0.247
L-shape	2.013	2.015	6.0×10^{-3}	2.024	2.008	1.837	1.838	5.8×10^{-3}	1.848	1.829
Hollow	0.547	0.547	1.8×10^{-4}	0.547	0.547	0.544	0.544	1.5×10^{-3}	0.548	0.542

To gain more insights into the performance and training dynamics of our approach, we visualize the loss histories and topology evolutions in Figs. 5a and 6, respectively (as loss curves are quite similar across the five cases, we only provide them for the MBB beam example). The curves for $L_P(\cdot)$ and $C_1^2(\cdot)$ with more fluctuations represent raw loss values recorded at each epoch, while the smoother dark-colored curves are the corresponding moving averaged versions. All three loss terms follow a similar trend: they rapidly increase early in the training, peaking around the 1000th epoch, followed by a gradual decrease toward their respective steady-state values. The potential energy loss $L_P(\cdot)$ remains strictly positive which is due to the regularization term $\tau(\cdot)$. The volume fraction constraint is effectively enforced as $C_1^2(\cdot)$ is consistently on the order of 10^{-5} after 5,000 of training epochs.

We can assess the force balance condition by examining the energy history curves shown in Fig. 5b. The strain energy and external work both initially rise from zero to their respective peaks, a trend that is similar to the loss trajectories. Small energy values indicate that the initial displacement fields are very small but these values rapidly increase as the optimization traverses through nontrivial displacement solutions. We observe a small mismatch between the two energy curves up to 2500 epochs, indicating that the force-balance condition has not yet been satisfied. In the following epochs, the curves gradually decrease and both

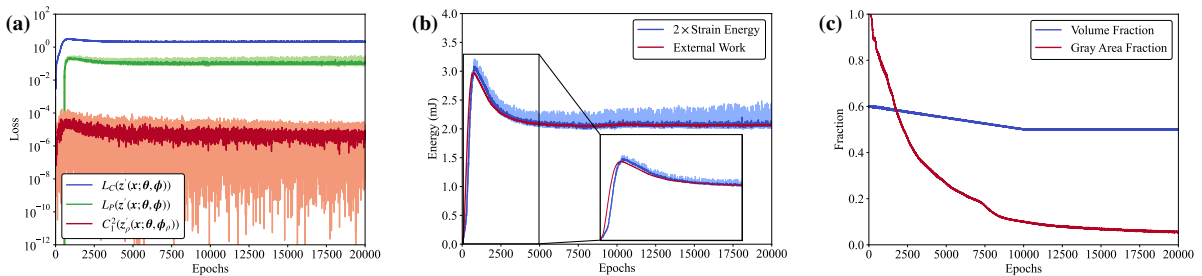


Fig. 5 Training dynamics in the MBB example: (a) evolution of the three loss terms, (b) convergence of the equilibrium condition shown by the agreement between $2 \times$ strain energy and the external work, (c) evolution of volume fraction and the gray area fraction. Similar trajectories are observed for other four benchmark examples.

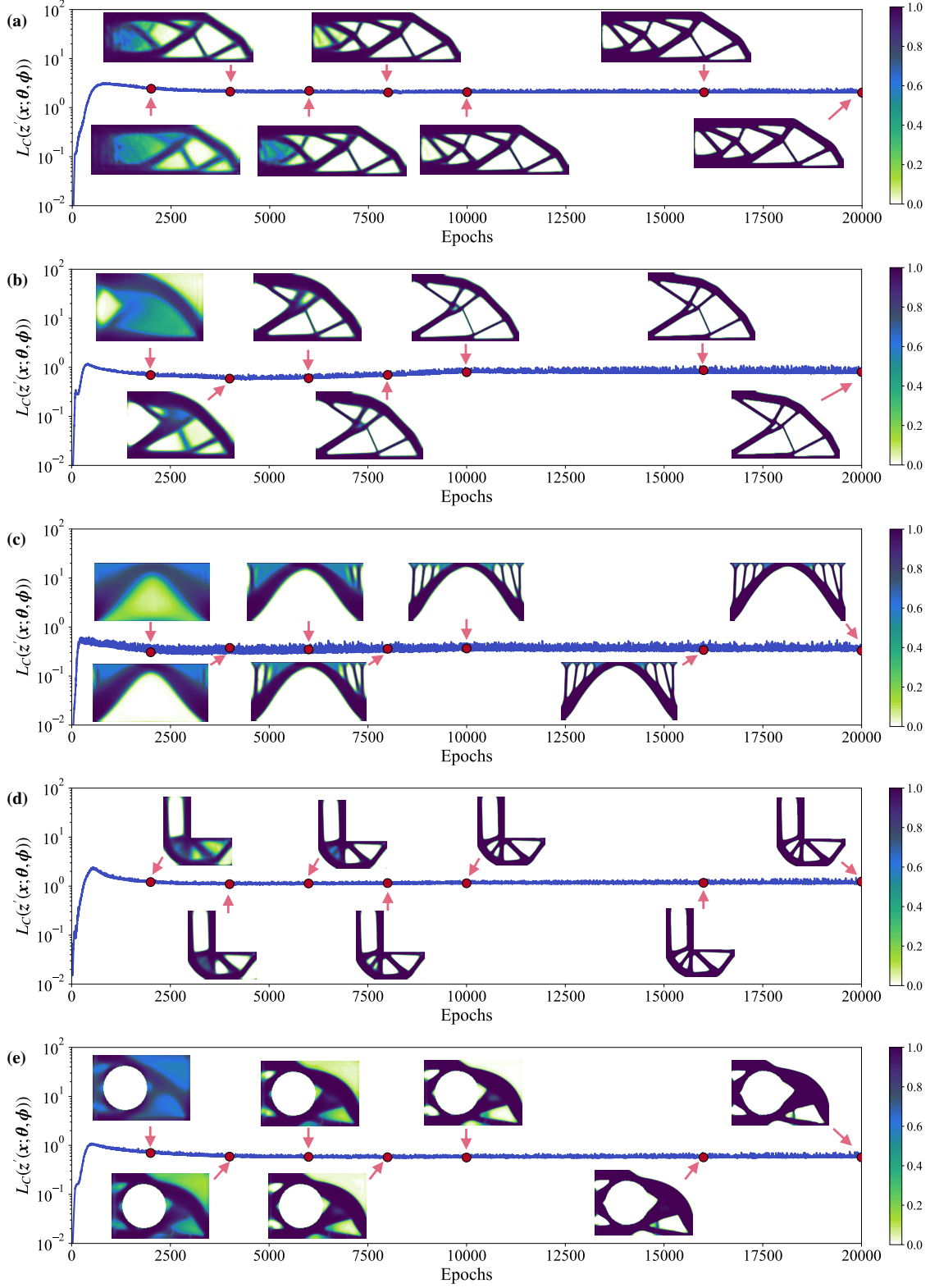


Fig. 6 Topology evolution throughout training: The median topologies at selected training epochs are visualized with respect to the objective $L_C(\cdot)$ for (a) MBB beam, (b) cantilever beam, (c) uniformly loaded beam, (d) L-shaped beam, and (e) hollow beam.

converge to $\sim 2\text{mJ}$ within 10,000 epochs. The achieved force-balance constraint is an essential condition for obtaining accurate displacement fields and topologies with smooth structural features.

As shown in Fig. 5c, the volume fraction history closely follows the curriculum training strategy of Section 3.3.2 in the first 50% of epochs, and remains constant thereafter. Concurrently, the gray area fraction drops rapidly during the first half of training and stays below 10% thereafter. This efficient reduction in gray regions further highlights the effectiveness of our PIGP framework in generating binary, well-defined topologies with minimal intermediate regions.

We present the evolution of the topologies for each example at selected training epochs in Fig. 6 (the topologies correspond to the median runs). We observe that in the early stage of training (around the 2000th epoch), the density field exhibits a large gray area with some discernible design features. A distinct topology emerges around the 4000th epoch in all examples, marking the onset of meaningful material redistribution. As training progresses, the overall structural layout stabilizes and the intermediate gray regions are gradually eliminated. By the end of training, the density field approaches a nearly binary distribution. Notably, high-quality topologies are often obtained with 10,000 epochs, indicating that the total computational cost can be reduced by half by adopting appropriate early stopping criteria.

4.2 Effects of PGCAN

To illustrate the effect of PGCAN compared to MLP, we first obtain the displacement and stress fields via the DEM (i.e., topology is fixed and not optimized). The potential energy $L_P(\cdot)$ is the only loss term, and the density field $\rho(\cdot)$ is uniformly prescribed to 1 in the entire domain except in the hole. FEM reference so-

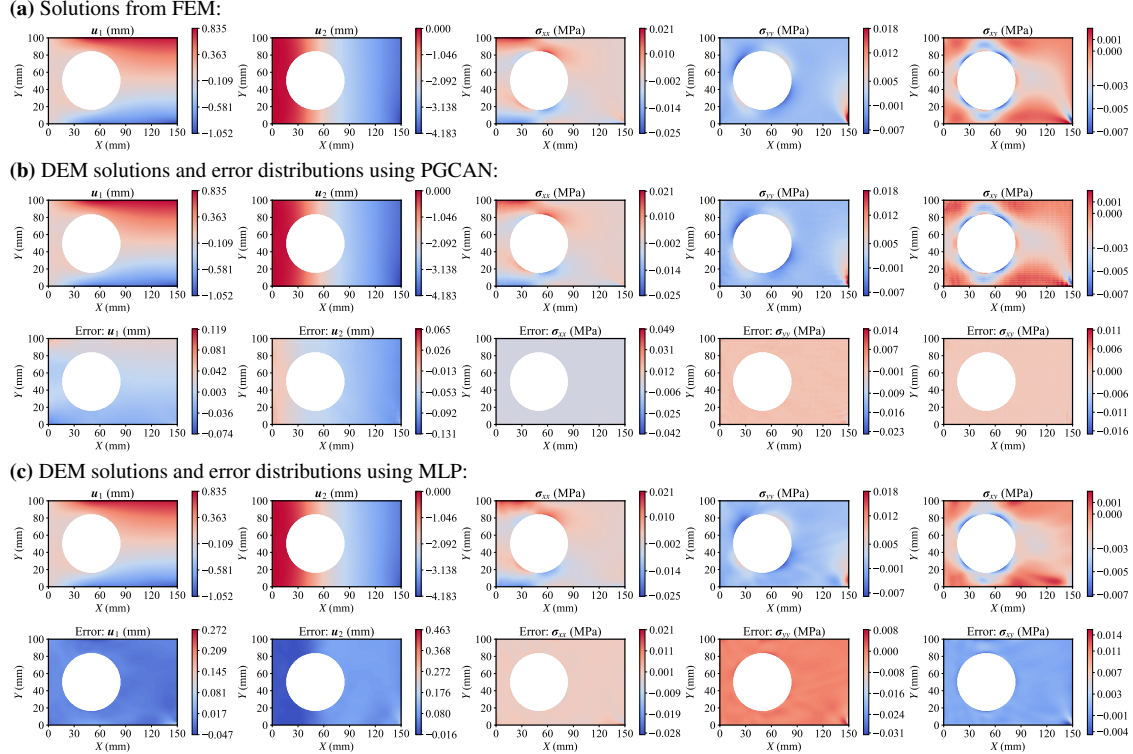


Fig. 7 Displacement and stress fields: (a) FEM reference solutions, (b) DEM solutions using PGCAN, and (c) DEM solutions using MLP. The corresponding error distributions relative to FEM are also presented.

lutions of displacements and stress components, along with the DEM solutions using PGCAN and MLP are shown in Fig. 7. Overall, both ML-based models produce displacement and stress fields that are comparable to the FEM reference but the displacement error distributions obtained from PGCAN are consistently lower than those from MLP. Due to the localized mechanism enforced by the feature encoder, PGCAN captures sharper and more realistic stress localizations than MLP near the external loading point or along the hole boundary.

The stress error plots in Fig. 7 may indicate that an MLP may outperform PGCAN in TO. To reject this statement, we visualize the energy histories in Fig. 8 where PGCAN and MLP stabilize and achieve equilibrium at epochs 200 and 1000, respectively. This large difference is due to PGCAN’s ability in capturing stress concentrations much faster than MLPs which suffer from spectral bias.

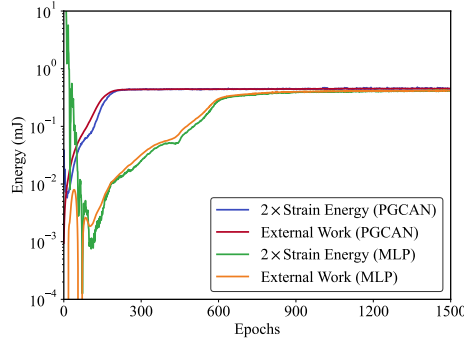


Fig. 8 Comparison of convergence rate to force balance condition: Evolution curves of $2\times$ strain energy and external work in the DEM using PGCAN are compared with those obtained using the MLP.

To further demonstrate the superiority of PGCAN over MLPs, we visualize the CM results for the uniformly loaded beam in Fig. 9. PGCAN effectively suppresses gray regions and yields a decent structure within 8000 epochs and the gray area is effectively minimized with 20,000 epochs. However, the MLP model fails to produce a discernible topology until the end of training and even then it provides an overly simplified structure with very high gray area fraction. This observation is consistent with the findings of [Chandrasekhar and Suresh \(2021\)](#) where MLPs were unable to solve this example due to the persistence of a large gray area fraction.

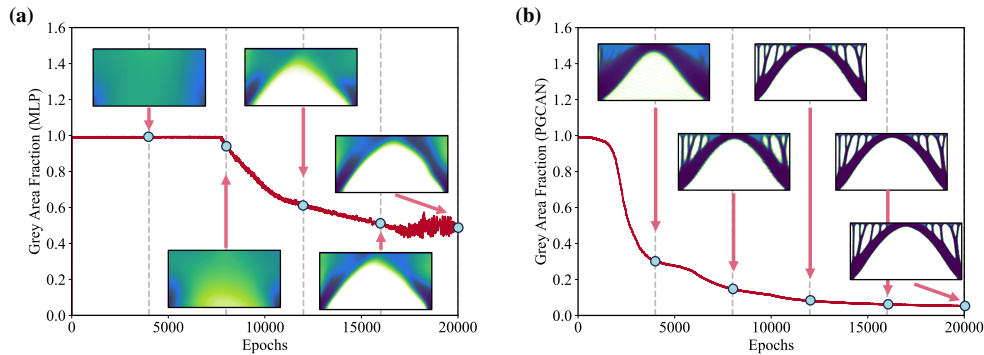


Fig. 9 Topology evolution for the uniformly loaded beam: Results from (a) MLP and (b) PGCAN with inset figures showing density distributions at selected epochs. PGCAN outperforms MLP in resolving fine design features.

4.3 Sensitivity Studies

To evaluate the robustness of our framework, we examine its sensitivity to three factors: (1) the resolution parameter Res in PGCAN, (2) the adaptive grid scheme, and (3) the curriculum training strategy introduced in Section 3.3.2. To assess the effect of Res on the resulting topologies, we consider the MBB beam example in Fig. 10, where Res is varied from 18 to 54. For comparison, we also include SIMP (Filter 2, 3 and 4) results initialized with random density fields. As shown in Fig. 10a, increasing Res leads to more intricate topological features. This behavior is attributed to the denser parameterization of the initial feature field F_0 at higher Res, which enhances the model’s ability to resolve finer spatial localizations.

To quantify the contribution of Res to structural complexity, we use median interface fractions as the metric. As shown in Fig. 10b, the median interface fraction is directly correlated to Res. The discrete points on this plot show that our PIGP framework produces structures spanning a wider range of interface fractions for each Res, including both simple and intricate designs. This variability is expected due to the inherent randomness in our ML-based approach from the initialization of θ and the adaptive grid strategy. In contrast, the interface fractions from SIMP locate within a narrower range for each filter size due to its deterministic formulation, where the only source of randomness is the initial density field.

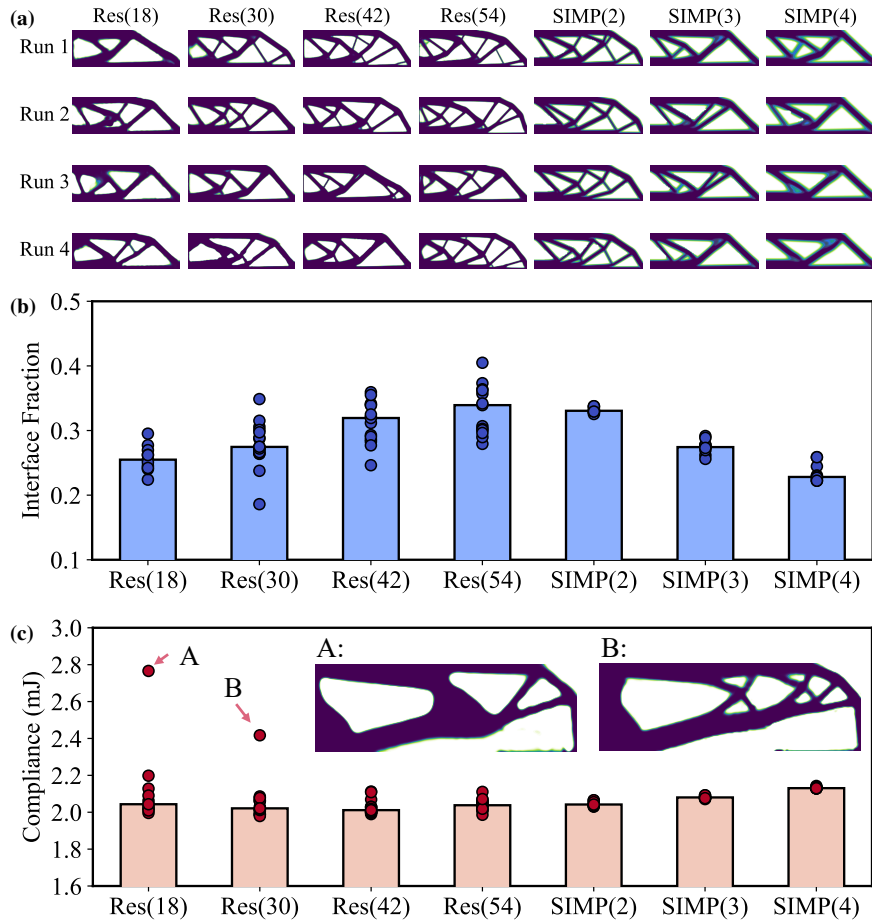


Fig. 10 Effect of Res on the MBB beam example: (a) Final topologies from PGCAN with Res ranging from 18 to 54, compared to SIMP results with varying filter radii; (b) comparison of interface fractions; and (c) comparison of compliance values. Outlier cases with elevated compliance at Res = 18 and Res = 30 are highlighted in the inset figures. The bar plots are made based on the median values across all repetitions.

We next compare the compliance values in Fig. 10c which shows that most topologies generated by our approach achieve median compliance values around 2.0, comparable to those from SIMP. However, two outlier cases exhibit significantly higher compliance, corresponding to suboptimal designs shown in the inset figures. These outliers reflect the broader design space explored by PIGP, which can yield less favorable solutions.

To examine the sensitivity to the adaptive grid scheme, we use the L-shape beam example with different sets of dynamic grids Σ . The results are summarized in Fig. 11a where SIMP baselines are also included for comparison. For each case, the coarse grid dimensions $(N_x^{(1)}, N_y^{(1)})$ are indicated in the subfigure titles, and the corresponding fine grid $(N_x^{(n_g)}, N_y^{(n_g)})$ doubles the cell resolution in both the x - and y -directions. For the SIMP cases, we consider three finite element grids (N_x, N_y) : (101, 101), (201, 201), and (301, 301), with scaled filter radius of 2, 4, and 6, respectively.

Fig. 11a shows that the topologies produced by our PIGP framework are insensitive to adaptive grid resolutions. This grid-independence is further supported by the median interface fraction results in Fig. 11b, which remain nearly constant across all PIGP cases. SIMP can also achieve similar mesh-independence by scaling the filter radius with the grid resolution. The median compliance values shown in Fig. 11c, indicate that our PIGP framework yields consistently lower and more broadly distributed compliance (most between 1.7 and 1.9) compared to SIMP which provides values that are concentrated around 2.0.

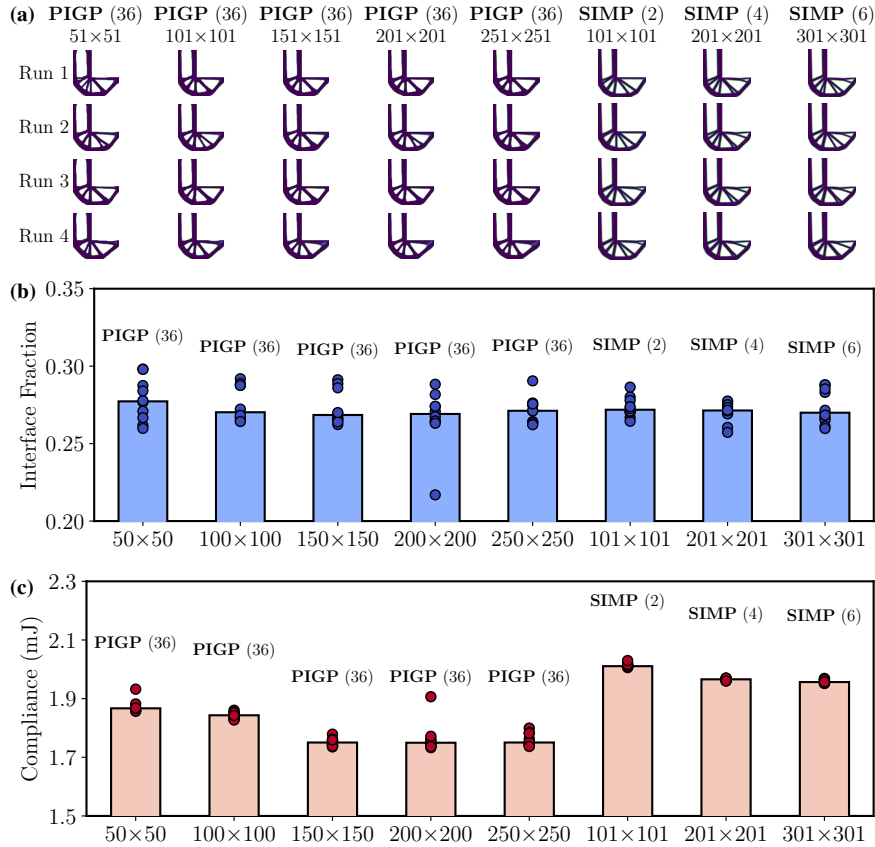


Fig. 11 Effect of grid resolutions for the L-shape beam: (a) Topologies using adaptive grid scheme with corresponding SIMP results; (b) comparison of interface fractions; and (c) compliance values across grid configurations. The bar plots are based on the median values.

Another factor that may influence the performance of our PIGP framework is the curriculum training schedule applied to the volume fraction constraint. We define the portion of the epochs where volume fraction is scheduled to decrease using γ in Equation (34). To assess the impact of γ , we evaluate the cantilever beam example with values ranging from 10% to 70% as shown in Fig. 12a along with the corresponding SIMP results. We observe that rapid volume fraction reduction (e.g., $\gamma = 10\%$) tends to produce topologies with fewer fine-scale features, whereas more gradual reductions (e.g., $\gamma \geq 30\%$) better preserve structural complexity. This behavior is quantitatively captured in the interface fractions shown in Fig. 12b. Additionally, increasing γ from 30% to 70% does not noticeably affect the median interface fraction, indicating that our approach remains robust to the choice of γ within this range.

We attribute the loss of fine features at small γ to the competition between $C_1^2(\cdot)$ and $L_P(\cdot)$. During the early training epochs, force equilibrium is not accurately satisfied which compromises the accuracy of stress and strain predictions in the localized regions associated with fine structural features. Our curriculum

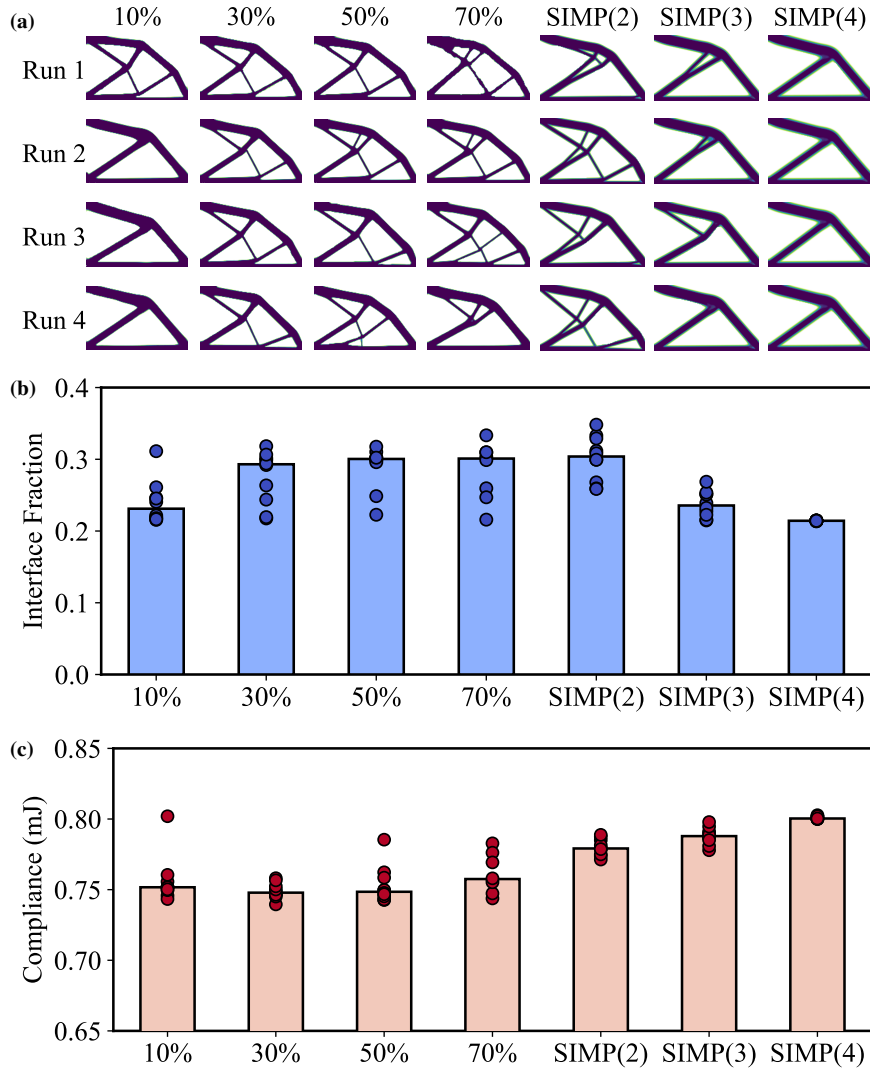


Fig. 12 Effect of curriculum training with scheduled volume fraction: (a) Final topologies for γ values ranging from 10% to 70%, shown alongside SIMP results; (b) comparison of interface fractions; and (c) corresponding compliance values. The bar plots use the median values.

training strategy mitigates this issue by gradually applying the volume fraction penalty; enabling the optimization to first focusing on converging to an accurate displacement solution and then satisfying the design constraint. As shown in Fig. 12c, the median compliance values across all γ cases from our approach are slightly lower than those obtained using SIMP, consistent with the results reported in Table 4.

4.4 Enforcing Design Features and Super-resolution

As discussed in Section 3.1, the GP formulation in our framework enables the direct specification of the design feature $\tilde{\rho}$ within designated regions of the domain. Additionally, our approach is mesh-free and provides a continuous representation of the state and design variables, i.e., we can visualize the fields with arbitrary resolution. To illustrate these capability, we present two examples by modifying the uniformly loaded beam and the hollow beam as shown in Fig. 13. For the uniformly loaded beam, we require a solid thin beam along the top edge to support the applied distributed load while in the hollow beam a solid circular ring is concentrically embedded around the hole.

We compare the topologies obtained from SIMP (Filter = 4) with those generated using our PIGP framework with Res = 18. Note that in SIMP, design features are enforced by assigning active or passive elements, whereas our PIGP framework achieves design constraints by sampling with GPs. The subtitles of the grid resolutions (N_x, N_y) in Fig. 13 indicate the number of CPs placed on the finite element mesh for SIMP, or on the structured grid used for *prediction* in our approach which used the adaptive grid resolution as listed in Table 2 during training.

For the uniformly loaded beam, SIMP produces large gray regions between the solid and void phases. In contrast, the structures generated by our approach have clean feature boundaries on both the (201, 101) and (401, 201) grids, with smoother surface for (401, 201). A similar trend is observed in the hollow beam example, where the void edge becomes smoother when using the denser (301, 201) grid to predict the density.

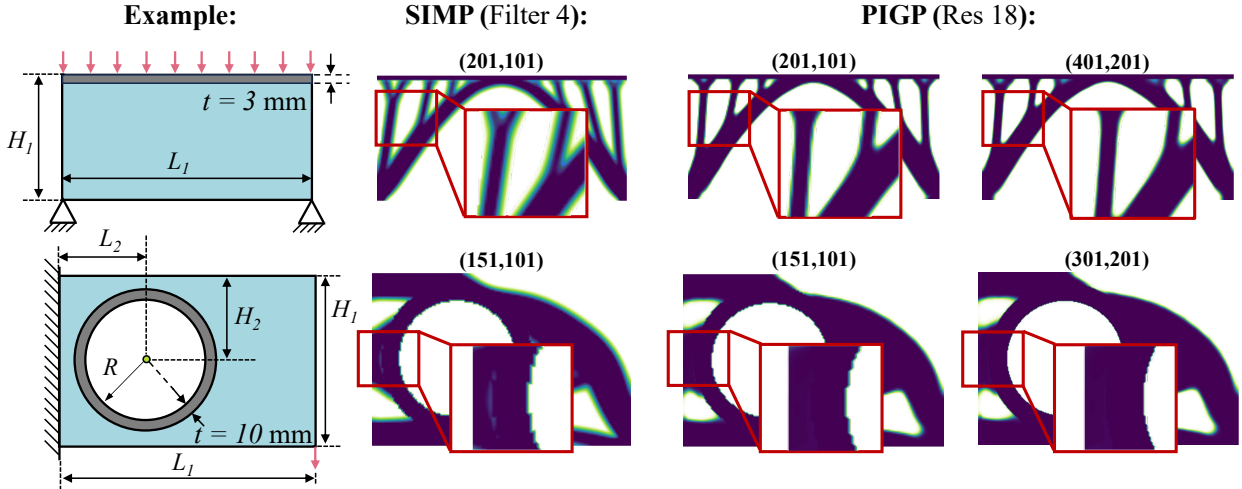


Fig. 13 Enforcing design features and super-resolution: The topology results obtained from SIMP (Filter 4) and PIGP (Res 18) are shown for the modified uniformly loaded and hollow beams. The uniformly loaded beam is required to have a solid thin beam underneath the distributed load while the hollow beam has a solid ring around its hole. The dimensions for the added design features are included and the rest (along with ψ_f) can be found in Table 1. Each figure includes a subtitle indicating the number of CPs (N_x, N_y) along the two spatial dimensions, which are positioned on the finite element mesh for SIMP, or on the structured grid for prediction in our PIGP framework. For our approach, we visualize the results (after training) at two grid resolutions to demonstrate its super-resolution capability (the pixels are artifacts of visualization).

While we learn a continuous representation for $\rho(\mathbf{x}; \boldsymbol{\theta}, \phi)$, SIMP directly updates a discrete density field defined on a fixed finite element mesh so it lacks the ability to naturally improve surface smoothness through resolution refinement. Across both examples we also observe that, unlike our approach, SIMP struggles to maintain strong connectivity across the regions where design constraints are enforced. In the uniformly loaded beam, there is weak connectivity between the top beam and the thin supporting structure. In the hollow beam example, SIMP solution shows a visible discontinuity at the interface between the solid ring and the surrounding material (see the zoomed-in figure).

4.5 Comparison of Computational Cost

To demonstrate the computational efficiency of our PIGP framework, we compare its runtime with several representative methods using the cantilever beam as the benchmark example. Specifically, we compare against: (1) SIMP implemented in MATLAB (Andreassen et al., 2011), (2) Topology Optimization using Neural Networks (TOuNN) (Chandrasekhar and Suresh, 2021), (3) the Deep Energy Method for Topology Optimization (DEMTOP) (He et al., 2023), and (4) the Complete Physics-Informed Neural Network for Topology Optimization (CPINNT0) (Jeong et al., 2023). Notably, all the four reference methods adopt a similar *nested* optimization strategy. It is worth noting that SIMP and TOuNN rely on FEM to compute the displacement fields, whereas DEMTOP and CPINNT0 employ the DEM.

To ensure a fair comparison, each reference method is implemented using a comparable mesh size and CP density. We use an adaptive grid scheme with the median intermediate grid matching that used in the other methods. Our PIGP framework and all other ML-based approaches are trained on the same GPU device.

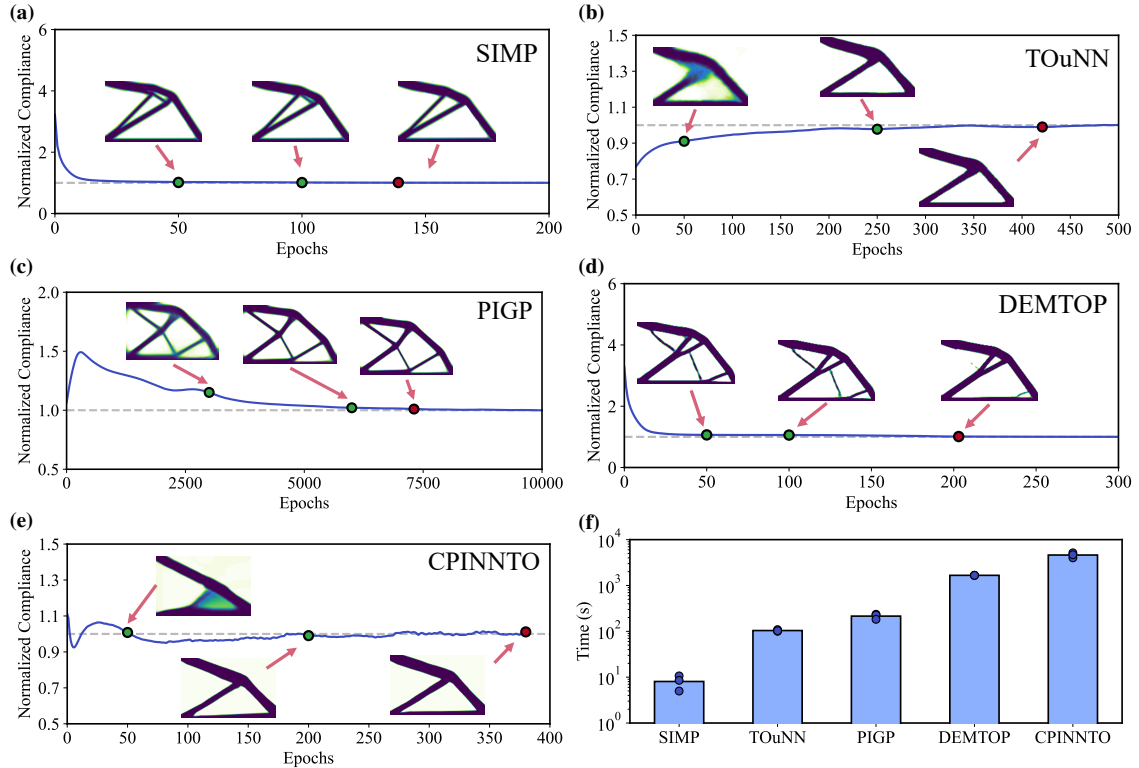


Fig. 14 Comparison of computational cost for the cantilever beam example: Normalized compliance histories for (a) SIMP, (b) TOuNN, (c) PIGP, (d) DEMTOP, and (e) CPINNT0, with intermediate and final topologies shown at selected epochs. (f) presents the total computational time at the point (red marker) where the final design criterion is met.

Due to differences in training objectives and optimization strategies, it is difficult to determine a consistent point at which the final optimal design is achieved across all methods. For instance, SIMP terminates when the maximum change in density between iterations falls below a specified threshold. However, this method is not directly applicable to ML-based approaches where local density variations can be large unless very small learning rates are used.

To ensure a consistent basis for comparison of computational time, we define a unified final design criterion based on normalized compliance histories. Each method is run for a sufficiently large number of epochs and the resulting compliance curve is smoothed using a moving average filter. The final smoothed compliance value is used to normalize the entire history, further reducing fluctuations. The final design and effective runtime are determined at the first epoch where the normalized compliance reaches 1.01 or 0.99, and stay within this range thereafter.

The normalized compliance curves for all five methods, each evaluated with three repetitions, are shown in Fig. 14a–Fig. 14e, along with the intermediate (green markers) and final (red markers) topologies. Among these methods, SIMP and DENTOP exhibit smoother compliance histories, which can be explained with the use of deterministic solvers such as MMA or OC. It is evident that high-quality designs are often achieved well before the final design criterion is met for all methods.

The total computational times required by each method at the final design point are summarized in Fig. 14f. As expected, SIMP is the most efficient, completing in approximately 10 seconds. TOuNN and our PIGP framework exhibit comparable runtimes, despite TOuNN relying on an efficient 2D FEM implementation to solve the displacement fields. Although both DENTOP and CPINNT0 also leverage DEM, their *nested* optimization strategies result in significantly longer runtimes, each exceeding 1000 seconds. This comparison underscores the computational efficiency of our *simultaneous* and mesh-free framework relative to more complex *nested* ML-based optimization pipelines such as DENTOP and CPINNT0.

5 Conclusions and Future Works

In this work, we propose a mesh-free physics-informed framework for density-based CM of solids. To parameterize the solution and design variables, our method employs independent GPs as priors with a shared multi-output NN as the mean function. We choose the PGCAN architecture as the mean function because of its ability to capture stress localization and fine-scale design features. By leveraging DEM, we reformulate the constrained CM problem with a *nested* structure into a computationally efficient and robust *simultaneous* and *mesh-free* optimization scheme. Our approach minimizes the compliance objective subject to two penalty terms that ensure the force balance and volume fraction constraints. Notably, no explicit penalty terms are required for BCs or design constraints, as these are inherently satisfied by the GP priors.

During model training, we incorporate an adaptive grid scheme along with the FD method for gradient evaluation to mitigate overfitting and enhance computational efficiency. Additionally, we adopt a curriculum training strategy with scheduling to prevent the volume fraction constraint from promoting overly simple topologies.

We tested our framework using canonical 2D examples and compared our results against SIMP. Our findings show that the proposed PIGP approach: (1) achieves lower compliance and reduces gray area fraction; (2) provides improved feature resolution and faster convergence with PGCAN compared to MLP; (3) effectively controls structural complexity through the interpretable parameter Res; (4) maintains grid-size independence without requiring a filtering technique; (5) can improve quality and continuity of topologies by leveraging GP sampling on a finer grid; and (6) offers higher computational efficiency compared to other

ML-based approaches that do not rely on FEM solvers.

Currently, our framework relies on the FD method for spatial gradient estimation, which offers computational efficiency but suffers from limited accuracy. Additionally, a large number of CPs is required to evaluate volume integrals in the loss functions. These limitations become more pronounced in 3D problems where the number of CPs can increase by an order of magnitude. A promising direction for the future work is the incorporation of interpolation-based techniques, such as shape functions from FEM, into the PIGP framework to reduce the number of CPs while maintaining high numerical fidelity and computational efficiency. Also, the computational cost can be further reduced, as completing all 20,000 epochs is often unnecessary for achieving final designs. We will pursue this direction in our future works.

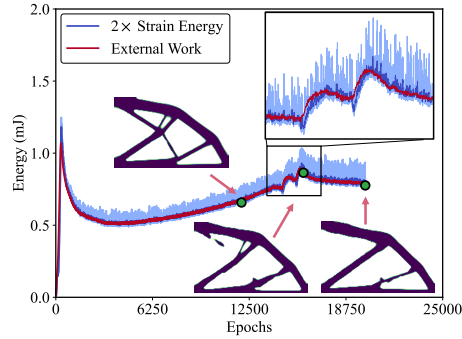


Fig. 15 Instability in the cantilever beam example: Evolution histories of $2\times$ strain energy and external work, with the inset highlighting their divergence, indicating a violation of the force balance constraint.

During the implementation of our framework, we occasionally observed training instabilities as illustrated in Fig. 15 using the cantilever beam example. At certain epochs, we observe an abrupt divergence between the curves of $2\times$ strain energy and external work (highlighted in the inset figure), indicating a breakdown in force equilibrium. This instability leads to degraded structural solutions, characterized by disconnected regions and irregular surfaces, where finer topological features are lost. While these instabilities can be detected early in training and mitigated via reinitialization, we aim to prevent them altogether in our future works.

Acknowledgments

We appreciate the support from the Office of the Naval Research (award number N000142312485), NASA’s Space Technology Research Grants Program (award number 80NSSC21K1809), and National Science Foundation (award number 2211908).

Declarations

Conflict of interest The authors declare that they have no conflicts of interest.

Replication of results The codes of the model are accessible via [GitHub](#) upon publication.

Appendix

A Nomenclature

Throughout this paper, we use regular, bold lowercase, and bold uppercase letters to denote scalars, vectors, and matrices, respectively. Vectors are assumed to be column. We distinguish between a function and its evaluations by explicitly showing functional dependence. For instance, $f(\mathbf{x})$ and $\mathbf{f}(\mathbf{x})$ represent scalar- and vector-valued functions, respectively.

When dealing with vector functions, we use subscripts for differentiation. As an example, the vector function of displacement $\mathbf{u}(\cdot)$ has two components denoted as $\mathbf{u}(\mathbf{x}) = [u_1(\mathbf{x}), u_2(\mathbf{x})]^T$. All functions are assumed to support batch evaluations; that is, a function $\mathbf{f}(\cdot)$ with n inputs and m outputs, applied to a matrix \mathbf{X} of n inputs (columns), returns a same-length matrix with m outputs (columns), i.e., $\mathbf{U} = \mathbf{f}(\mathbf{X})$. Key symbols and their definitions are provided in Table 5 with more symbols specified in each section.

Table 5 Summary of key notations: More symbols and notations are given in each section.

Symbols	Description
θ	Set of all trainable NN parameters
\mathbf{x}	Coordinates of a spatial point
\mathbf{X}	A set of CPs
$\rho(\mathbf{x})$	Density function
$\mathbf{u}(\cdot), u_1(\cdot), u_2(\cdot)$	Displacement functions
$\tilde{\mathbf{u}}_1, \tilde{\mathbf{u}}_2, \tilde{\rho}$	BCs for displacement and density
$\boldsymbol{\sigma}(\mathbf{x}), \boldsymbol{\varepsilon}(\mathbf{x})$	Stress and strain tensors
$\hat{\boldsymbol{\varepsilon}}(\mathbf{x})$	Strain with no gradients
$\mathbf{f}(\mathbf{x})$	External force
$\mathbf{C}(\mathbf{x})$	Elastic stiffness tensor
E_{\max}, E_{\min}	Young’s modulus for solids and void
ν	Poisson’s ratio
p	Penalization factor
$\Omega, \Omega_{\mathbf{u}}, \Omega_F$	Design domain and boundaries
α_0, α_1	Weight factors for loss terms

B Numerical Differentiation with Finite Difference Method

We use the FD method on a structured grid to compute spatial derivatives (Nocedal and Wright, 2006). Taking the horizontal displacement $u_1(\mathbf{x})$ as an example, the gradients at the query point $[x_i, y_j]$ using the

FD method can be written as:

$$\frac{\partial u_1(x_i, y_j)}{\partial x} \approx \frac{u_1(x_{i+1}, y_j) - u_1(x_{i-1}, y_j)}{2dx}, \quad (36a)$$

$$\frac{\partial^2 u_1(x_i, y_j)}{\partial x^2} \approx \frac{u_1(x_{i+1}, y_j) - 2u_1(x_i, y_j) + u_1(x_{i-1}, y_j)}{dx^2}, \quad (36b)$$

$$\frac{\partial^2 u_1(x_i, y_j)}{\partial x \partial y} \approx \frac{u_1(x_{i+1}, y_{j+1}) - u_1(x_{i+1}, y_{j-1}) - u_1(x_{i-1}, y_{j+1}) + u_1(x_{i-1}, y_{j-1})}{4dx dy}, \quad (36c)$$

where dx and dy are the intervals between grid points in the x - and y -directions, respectively, and subscripts $i \in [1, N_x], j \in [1, N_y]$ denotes adjacent points in a structured grid. Similar formulations can be derived for the partial derivatives with respect to y .

We can estimate the residuals of the governing PDEs using Equation (36). To begin with, the constitutive relations in Equation (6) can be explicitly written as:

$$\sigma_{xx}(\mathbf{x}) = \frac{E(\mathbf{x})}{1 - \nu^2} (\varepsilon_{xx}(\mathbf{x}) + \nu \varepsilon_{yy}(\mathbf{x})), \quad (37a)$$

$$\sigma_{yy}(\mathbf{x}) = \frac{E(\mathbf{x})}{1 - \nu^2} (\nu \varepsilon_{xx}(\mathbf{x}) + \varepsilon_{yy}(\mathbf{x})), \quad (37b)$$

$$\sigma_{xy}(\mathbf{x}) = \frac{E(\mathbf{x})}{1 + \nu} \varepsilon_{xy}(\mathbf{x}), \quad (37c)$$

where $\sigma_{xx}(\mathbf{x})$, $\sigma_{yy}(\mathbf{x})$, $\sigma_{xy}(\mathbf{x})$, $\varepsilon_{xx}(\mathbf{x})$, $\varepsilon_{yy}(\mathbf{x})$, and $\varepsilon_{xy}(\mathbf{x})$ are the independent components for the stress and strain tensors.

Using Equation (4) and Equation (37), we can rewrite the governing equation in Equation (2) as two PDE residuals:

$$R_{\text{PDE1}}(\mathbf{x}) = \frac{E(\mathbf{x})}{1 - \nu^2} \frac{\partial^2 u_1(\mathbf{x})}{\partial x^2} + \frac{E(\mathbf{x})}{2(1 + \nu)} \frac{\partial^2 u_1(\mathbf{x})}{\partial y^2} + \left[\frac{E(\mathbf{x})\nu}{1 - \nu^2} + \frac{E(\mathbf{x})}{2(1 + \nu)} \right] \frac{\partial^2 u_2(\mathbf{x})}{\partial x \partial y}, \quad (38a)$$

$$R_{\text{PDE2}}(\mathbf{x}) = \frac{E(\mathbf{x})}{2(1 + \nu)} \frac{\partial^2 u_2(\mathbf{x})}{\partial x^2} + \frac{E(\mathbf{x})}{1 - \nu^2} \frac{\partial^2 u_2(\mathbf{x})}{\partial y^2} + \left[\frac{E(\mathbf{x})\nu}{1 - \nu^2} + \frac{E(\mathbf{x})}{2(1 + \nu)} \right] \frac{\partial^2 u_1(\mathbf{x})}{\partial x \partial y}, \quad (38b)$$

where the displacement gradient terms can be estimated with Equation (36). The PDE losses (L_{PDE1} and L_{PDE2}) are defined as the mean squared errors of the residuals in Equation (38a) and Equation (38b) on all CPs.

C Length-scale Parameter in Gaussian Processes

In this study, we adopt a heuristic procedure to select the length-scale parameter ϕ_ρ . As illustrated in Fig. 16, we parameterize the density field for the hollow beam structure consisting of a solid ring enclosing a central hole. The design constraints are enforced using GPs by varying ϕ_ρ from 3.0 to 0.5. The GP kernels are defined over a structured grid with $N_x = 151$ and $N_y = 101$.

We use PGCAN as the network architecture to predict the density fields on three structured grids: $(N_x, N_y) = (151, 101)$, $(226, 151)$, and $(301, 201)$, corresponding to the three columns from left to right in Fig. 16. No training is conducted in this analysis, and the predicted density field is evaluated through a single forward pass. The GP-enforced field is expected to satisfy the prescribed density constraints independently of the network parameters θ or the grid resolutions.

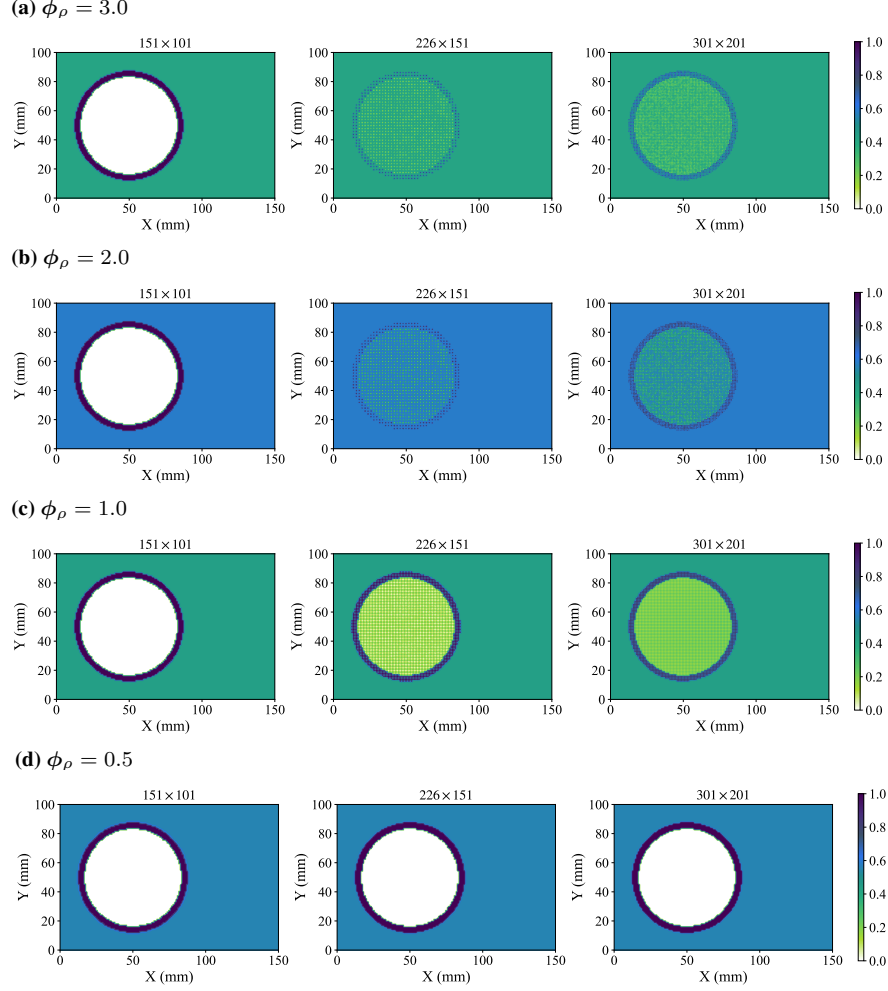


Fig. 16 Effect of length-scale parameter ϕ_ρ on density parameterization: Density fields generated by a PGCAN model before training. The GP interpolations with different values of ϕ_ρ is applied to prescribed densities along the solid ring and the central void

As shown in Fig. 16, all four models successfully reconstruct the intended structure when evaluated on the coarse grid with the resolution of (151, 101), which is expected, as the predictions with GP are conditioned on this grid. However, when evaluated on finer grids such as (226, 151) or (301, 201) with ϕ_ρ greater than 0.5, regions that are expected to be fully solid ($\rho(\mathbf{x}) = 1$) or entirely void ($\rho(\mathbf{x}) = 0$) exhibit large deviations from the prescribed values. These inaccuracies are particularly problematic in the context of adaptive grid scheme, where CPs are dynamically sampled.

We can use small values of ϕ_ρ to mitigate this issue. From Fig. 16d, we observe that the parameter $\phi_\rho = 0.5$ reliably reconstructs the desired structural features across all three grids. Since we define the grid resolutions consistently in table 2, and all GPs are sampled with the coarse grids, we set the length-scale parameter $\phi = 0.5$, and expect that the displacement BCs and design constraint can be naturally satisfied for all grids in the adaptive grid scheme.

D Effects from Adaptive Grids

The model with PGCAN must be trained using an adaptive grid scheme to mitigate overfitting. Fig. 17a shows the horizontal displacement u_1 obtained from training with CPs placed on a fixed structured grid, where overfitting appears as vertical stripe patterns as highlighted in the inset. These stripe features exhibit high local gradient magnitudes. As the comparison, the horizontal displacement field obtained from the adaptive grid scheme in Fig. 17b is smoother and more physically reasonable.

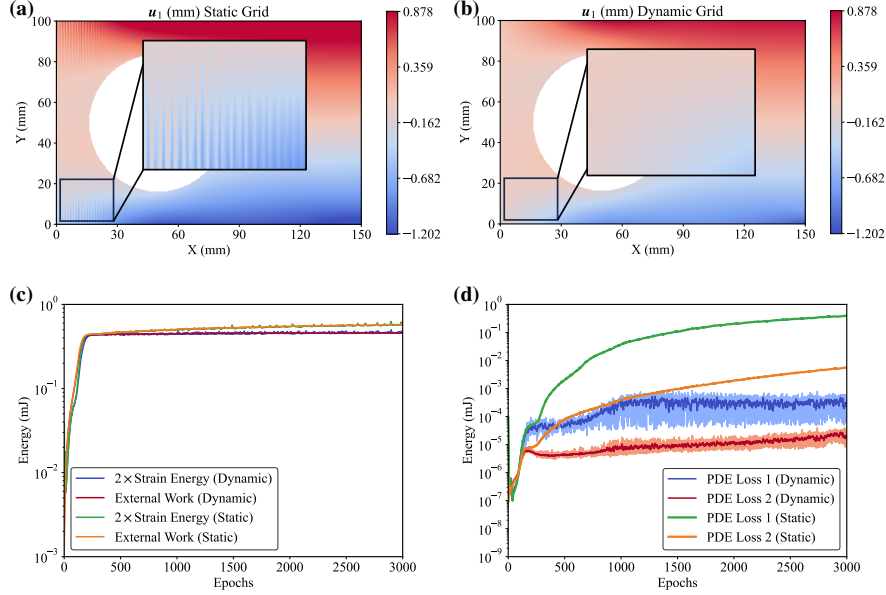


Fig. 17 Comparison of DEM results using PGCAN with static and adaptive grid schemes: (a) horizontal displacement distribution obtained using the static grid, (b) the corresponding distribution computed with the adaptive grid scheme, (c) evolution histories of strain energy and external work for both schemes, and (d) loss histories of the PDE residuals. A zoomed-in region in (a) highlights the overfitting issue.

Our proposed adaptive training strategy also improves robustness in the overall training dynamics. As shown in Fig. 17c, both training schemes reach force equilibrium around the 200th epoch, while the adaptive grid scheme has the two curves (the $2 \times$ strain energy and external work) closely aligned and stabilized. However, the static grid exhibits a growing trend of these two curves, indicating the progressive overfitting. This divergence behavior is further illustrated by the loss histories of the two PDE residuals⁵ shown in Fig. 17d, where the adaptive grid remains stable with low residuals on the order of 10^{-4} , while those in the static grid case steadily increase, leading to significant PDE errors.

E Interface Fraction

The interface fraction is defined as the ratio of the number of interface pixels to the total number of solid pixels. This metric is inherently sensitive to the grid resolution. To be consistent, we interpolate the predicted density fields onto their respective coarse grids and then estimate the interface fractions.

To quantify the interface fraction, we apply image processing techniques to the final topologies of all examples. We first binarize the topology using a thresholding technique to remove any gray pixels. The

⁵Additional details on computing PDE residuals are provided in Appendix B.

threshold value is iteratively adjusted until the resulting binary structure satisfies the prescribed volume fraction constraint. Morphological operations of erosion and dilation are then applied to the binarized structure to identify interface pixels (green) as illustrated in Fig. 18 for the MBB beam and cantilever beam examples.

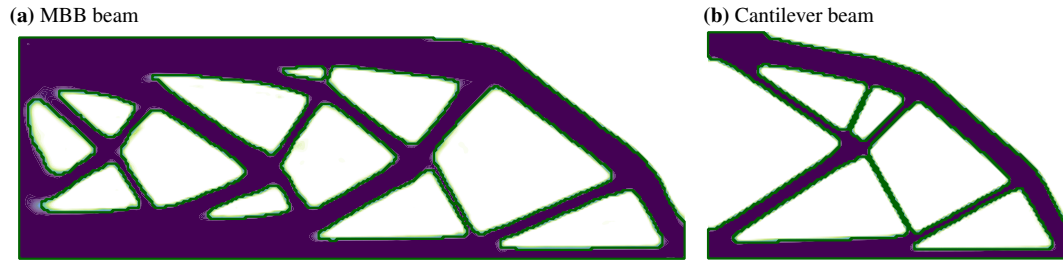


Fig. 18 Interface extraction in final topologies: Examples from (a) the MBB beam and (b) the cantilever beam are visualized with the interface pixels highlighted in green.

References

- Bendsøe, M.P., Kikuchi, N.: Generating optimal topologies in structural design using a homogenization method. *Computer Methods in Applied Mechanics and Engineering* **71**(2), 197–224 (1988) [https://doi.org/10.1016/0045-7825\(88\)90086-2](https://doi.org/10.1016/0045-7825(88)90086-2)
- Bendsøe, M.P.: *Optimization of Structural Topology, Shape, and Material*. Springer, Berlin, Heidelberg (1995). <https://doi.org/10.1007/978-3-662-03115-5>. <http://link.springer.com/10.1007/978-3-662-03115-5>
- Borrvall, T., Petersson, J.: Topology optimization of fluids in Stokes flow. *International Journal for Numerical Methods in Fluids* **41**(1), 77–107 (2003) <https://doi.org/10.1002/flid.426>
- Bendsøe, M.P., Sigmund, O.: *Topology Optimization: Theory, Methods, and Applications*. Springer, Berlin, Heidelberg (2004). <https://doi.org/10.1007/978-3-662-05086-6>. <http://link.springer.com/10.1007/978-3-662-05086-6>
- Wang, C., Zhao, Z., Zhou, M., Sigmund, O., Zhang, X.S.: A comprehensive review of educational articles on structural and multidisciplinary optimization. *Structural and Multidisciplinary Optimization* **64**(5), 2827–2880 (2021) <https://doi.org/10.1007/s00158-021-03050-7>
- Sigmund, O.: A 99 line topology optimization code written in Matlab. *Structural and Multidisciplinary Optimization* **21**(2), 120–127 (2001) <https://doi.org/10.1007/s001580050176>
- Andreassen, E., Clausen, A., Schevenels, M., Lazarov, B.S., Sigmund, O.: Efficient topology optimization in MATLAB using 88 lines of code. *Structural and Multidisciplinary Optimization* **43**(1), 1–16 (2011) <https://doi.org/10.1007/s00158-010-0594-7>
- Liu, K., Tovar, A.: An efficient 3D topology optimization code written in Matlab. *Structural and Multidisciplinary Optimization* **50**(6), 1175–1196 (2014) <https://doi.org/10.1007/s00158-014-1107-x>

- Chen, F., Wang, Y., Wang, M.Y., Zhang, Y.F.: Topology optimization of hyperelastic structures using a level set method. *Journal of Computational Physics* **351**, 437–454 (2017) <https://doi.org/10.1016/j.jcp.2017.09.040>
- Wu, J., Sigmund, O., Groen, J.P.: Topology optimization of multi-scale structures: a review. *Structural and Multidisciplinary Optimization* **63**(3), 1455–1480 (2021) <https://doi.org/10.1007/s00158-021-02881-8>
- Zhao, Z., Zhang, X.S.: Design of graded porous bone-like structures via a multi-material topology optimization approach. *Structural and Multidisciplinary Optimization* **64**(2), 677–698 (2021) <https://doi.org/10.1007/s00158-021-02870-x>
- Zhai, X., Wang, W., Chen, F., Wu, J.: Topology optimization of differentiable microstructures. *Computer Methods in Applied Mechanics and Engineering* **418**, 116530 (2024) <https://doi.org/10.1016/j.cma.2023.116530>
- Senhora, F.V., Giraldo-Londoño, O., Menezes, I.F.M., Paulino, G.H.: Topology optimization with local stress constraints: a stress aggregation-free approach. *Structural and Multidisciplinary Optimization* **62**(4), 1639–1668 (2020) <https://doi.org/10.1007/s00158-020-02573-9>
- Jia, Y., Lopez-Pamies, O., Zhang, X.S.: Controlling the fracture response of structures via topology optimization: From delaying fracture nucleation to maximizing toughness. *Journal of the Mechanics and Physics of Solids* **173**, 105227 (2023) <https://doi.org/10.1016/j.jmps.2023.105227>
- Svanberg, K.: The method of moving asymptotes—a new method for structural optimization. *International Journal for Numerical Methods in Engineering* **24**(2), 359–373 (1987) <https://doi.org/10.1002/nme.1620240207>
- Shin, S., Shin, D., Kang, N.: Topology optimization via machine learning and deep learning: a review. *Journal of Computational Design and Engineering* **10**(4), 1736–1766 (2023) <https://doi.org/10.1093/jcde/qwad072>
- Chi, H., Zhang, Y., Tang, T.L.E., Mirabella, L., Dalloro, L., Song, L., Paulino, G.H.: Universal machine learning for topology optimization. *Computer Methods in Applied Mechanics and Engineering* **375**, 112739 (2021) <https://doi.org/10.1016/j.cma.2019.112739>
- Senhora, F.V., Chi, H., Zhang, Y., Mirabella, L., Tang, T.L.E., Paulino, G.H.: Machine learning for topology optimization: Physics-based learning through an independent training strategy. *Computer Methods in Applied Mechanics and Engineering* **398**, 115116 (2022) <https://doi.org/10.1016/j.cma.2022.115116>
- Yamasaki, S., Yaji, K., Fujita, K.: Data-driven topology design using a deep generative model. *Structural and Multidisciplinary Optimization* **64**(3), 1401–1420 (2021) <https://doi.org/10.1007/s00158-021-02926-y>. Accessed 2025-06-14
- Sim, E.-A., Lee, S., Oh, J., Lee, J.: GANs and DCGANs for generation of topology optimization validation curve through clustering analysis. *Advances in Engineering Software* **152**, 102957 (2021) <https://doi.org/10.1016/j.advengsoft.2020.102957>. Accessed 2025-06-14
- Kallioras, N.A., Lagaros, N.D.: MLGen: Generative Design Framework Based on Machine Learning and Topology Optimization. *Applied Sciences* **11**(24), 12044 (2021) <https://doi.org/10.3390/app112412044>. Accessed 2025-06-14

- Nie, Z., Lin, T., Jiang, H., Kara, L.B.: TopologyGAN: Topology Optimization Using Generative Adversarial Networks Based on Physical Fields Over the Initial Domain. *Journal of Mechanical Design* **143**(3), 031715 (2021) <https://doi.org/10.1115/1.4049533> . Accessed 2025-06-14
- Nguyen-Thanh, V.M., Zhuang, X., Rabczuk, T.: A deep energy method for finite deformation hyperelasticity. *European Journal of Mechanics - A/Solids* **80**, 103874 (2020) <https://doi.org/10.1016/j.euromechsol.2019.103874>
- He, J., Abueidda, D., Abu Al-Rub, R., Koric, S., Jasiuk, I.: A deep learning energy-based method for classical elastoplasticity. *International Journal of Plasticity* **162**, 103531 (2023) <https://doi.org/10.1016/j.ijplas.2023.103531>
- Hamel, C.M., Long, K.N., Kramer, S.L.B.: Calibrating constitutive models with full-field data via physics informed neural networks. *Strain* **59**(2), 12431 (2023) <https://doi.org/10.1111/str.12431>
- Niu, S., Zhang, E., Bazilevs, Y., Srivastava, V.: Modeling finite-strain plasticity using physics-informed neural network and assessment of the network performance. *Journal of the Mechanics and Physics of Solids* **172**, 105177 (2023) <https://doi.org/10.1016/j.jmps.2022.105177>
- Fuhg, J.N., Bouklas, N.: The mixed Deep Energy Method for resolving concentration features in finite strain hyperelasticity. *Journal of Computational Physics* **451**, 110839 (2022) <https://doi.org/10.1016/j.jcp.2021.110839>
- Hoyer, S., Sohl-Dickstein, J., Greydanus, S.: Neural reparameterization improves structural optimization. *arXiv. arXiv:1909.04240 [cs, stat]* (2019). <http://arxiv.org/abs/1909.04240>
- Chandrasekhar, A., Suresh, K.: TOuNN: Topology Optimization using Neural Networks. *Structural and Multidisciplinary Optimization* **63**(3), 1135–1149 (2021) <https://doi.org/10.1007/s00158-020-02748-4>
- Chandrasekhar, A., Suresh, K.: Approximate Length Scale Filter in Topology Optimization using Fourier Enhanced Neural Networks. *Computer-Aided Design* **150**, 103277 (2022) <https://doi.org/10.1016/j.cad.2022.103277>
- He, J., Chadha, C., Kushwaha, S., Koric, S., Abueidda, D., Jasiuk, I.: Deep energy method in topology optimization applications. *Acta Mechanica* **234**(4), 1365–1379 (2023) <https://doi.org/10.1007/s00707-022-03449-3>
- Yin, J., Wen, Z., Li, S., Zhang, Y., Wang, H.: Dynamically configured physics-informed neural network in topology optimization applications. *Computer Methods in Applied Mechanics and Engineering* **426**, 117004 (2024) <https://doi.org/10.1016/j.cma.2024.117004>
- Zhao, X., Mezzadri, F., Wang, T., Qian, X.: Physics-informed neural network based topology optimization through continuous adjoint. *Structural and Multidisciplinary Optimization* **67**(8), 143 (2024) <https://doi.org/10.1007/s00158-024-03856-1>
- Zehnder, J., Li, Y., Coros, S., Thomaszewski, B.: NTopo: Mesh-free Topology Optimization using Implicit Neural Representations (2021). <https://arxiv.org/abs/2102.10782>
- Joglekar, A., Chen, H., Kara, L.B.: DMF-TONN: Direct Mesh-free Topology Optimization using Neural Networks. *Engineering with Computers* **40**(4), 2227–2240 (2024) <https://doi.org/10.1007/s00366-023-01904-w>

- Jeong, H., Batuwatta-Gamage, C., Bai, J., Xie, Y.M., Rathnayaka, C., Zhou, Y., Gu, Y.: A complete Physics-Informed Neural Network-based framework for structural topology optimization. *Computer Methods in Applied Mechanics and Engineering* **417**, 116401 (2023) <https://doi.org/10.1016/j.cma.2023.116401>
- Cuomo, S., Di Cola, V.S., Giampaolo, F., Rozza, G., Raissi, M., Piccialli, F.: Scientific Machine Learning Through Physics-Informed Neural Networks: Where we are and What's Next. *Journal of Scientific Computing* **92**(3), 88 (2022) <https://doi.org/10.1007/s10915-022-01939-z>
- Kang, N., Lee, B., Hong, Y., Yun, S.-B., Park, E.: PIXEL: Physics-Informed Cell Representations for Fast and Accurate PDE Solvers. *Proceedings of the AAAI Conference on Artificial Intelligence* **37**(7), 8186–8194 (2023) <https://doi.org/10.1609/aaai.v37i7.25988>
- Rao, C., Sun, H., Liu, Y.: Physics-Informed Deep Learning for Computational Elastodynamics without Labeled Data. *Journal of Engineering Mechanics* **147**(8), 04021043 (2021) [https://doi.org/10.1061/\(ASCE\)EM.1943-7889.0001947](https://doi.org/10.1061/(ASCE)EM.1943-7889.0001947)
- Nocedal, J., Wright, S.J.: *Numerical Optimization*, 2nd ed edn. Springer series in operations research. Springer, New York (2006). OCLC: ocm68629100
- Wang, F., Lazarov, B.S., Sigmund, O.: On projection methods, convergence and robust formulations in topology optimization. *Structural and Multidisciplinary Optimization* **43**(6), 767–784 (2011) <https://doi.org/10.1007/s00158-010-0602-y>
- Mora, C., Yousefpour, A., Hosseinmardi, S., Bostanabad, R.: A gaussian process framework for solving forward and inverse problems involving nonlinear partial differential equations. *Computational Mechanics* (2024) <https://doi.org/10.1007/s00466-024-02559-0>
- Yousefpour, A., Hosseinmardi, S., Mora, C., Bostanabad, R.: Simultaneous and meshfree topology optimization with physics-informed Gaussian processes. *Computer Methods in Applied Mechanics and Engineering* **437**, 117698 (2025) <https://doi.org/10.1016/j.cma.2024.117698>
- Shishehbor, M., Hosseinmardi, S., Bostanabad, R.: Parametric encoding with attention and convolution mitigate spectral bias of neural partial differential equation solvers. *Structural and Multidisciplinary Optimization* **67**(7), 128 (2024) <https://doi.org/10.1007/s00158-024-03834-7>
- Soviany, P., Ionescu, R.T., Rota, P., Sebe, N.: Curriculum Learning: A Survey. *International Journal of Computer Vision* **130**(6), 1526–1565 (2022) <https://doi.org/10.1007/s11263-022-01611-x>. Accessed 2025-06-16
- Yousefpour, A., Hosseinmardi, S., Sun, X., Bostanabad, R.: Localized physics-informed gaussian processes with curriculum training for topology optimization. *ArXiv* **abs/2503.15561** (2025)